



Project of Strategic Interest NEXTDATA

Deliverable D2.6.2: Results of the pilot studies

Author: Elisa Palazzi
CNR-ISAC

D2.6.2a: “Analysis of water resources in the Himalaya-Karakorum and interaction between monsoon and mid-latitude perturbations”

Author: E. Palazzi
CNR-ISAC, Torino

Contributors:
J. von Hardenberg, A. Provenzale, L. Filippi, S. Terzago
CNR-ISAC, Torino

This Deliverable is structured in two sections, followed by a final part summarizing the progresses and outcomes of the pilot study during the second year of activity (2013).

The first section describes the characteristics of the current and future precipitation in the Hindu-Kush Karakoram Himalaya (HKKH) region inferred from an ensemble of global climate models included in the Coupled Model Intercomparison Project Phase 5 (CMIP5) Archive.

The second section focuses on the western portion of the HKKH domain, namely the Hindu-Kush Karakoram (HKK), and presents an analysis of the synoptic origin and driving mechanisms of winter precipitation in this area.

1. The CMIP5 picture of current and future precipitation in the Karakoram-Himalaya

The simulation and projection of precipitation by means of global climate models (GCMs) in mountain areas are affected by large uncertainties because the controls of topography on precipitation are still not properly represented in this class of models, mainly as an effect of their coarse spatial resolution.

Processes affecting precipitation in the Hindu-Kush Karakoram Himalaya (HKKH), one of the most important mountain regions of the world, are very complex, due to the variety of meteorological regimes and interaction of local and large-scale circulation systems, resulting in large variability and lack of spatial coherence in the observed precipitation trends (e.g., Solomon et al, 2007). Two main sub-regions, prone to the influence of different circulation patterns, can be distinguished in this region. The western Hindu-Kush Karakoram (HKK) area is largely exposed to the arrival of westerly perturbations bringing precipitation during Winter and early Spring and is less affected by the monsoon circulation, while the eastern Himalaya region is exposed to the summer monsoon precipitation (Syed et al, 2006; Yadav et al, 2012).

In a previous study (Palazzi et al, 2013), an important outcome of the first year NextData activities, we have analysed the properties of precipitation in the HKKH region by using various precipitation datasets including satellite rainfall estimates, reanalysis data, gridded in situ rain gauge data, and a merged satellite and rain gauge climatology, to analyse precipitation at the seasonal scale in terms of area averages over the HKK and the Himalayan regions. We compared the observation-based and reanalysis data to the output of one state-of-the-art GCM, EC-Earth (Hazeleger et al, 2012), to evaluate to which extent this specific GCM is able to reproduce precipitation patterns, seasonality, and long-

term behaviour in the two sub-regions of the HKKH, in spite of its coarse spatial resolution, and to evaluate future seasonal precipitation trends under different forcing conditions.

During the second year we have extended the model analysis discussed in our former study to an ensemble of thirty-two GCMs participating in the World Climate Research Program (WCRP) Coupled Model Intercomparison Project Phase 5 (CMIP5), in order to 1) provide an overview of the performance of these models in simulating the current and future precipitation climatology and trends in the HKK and Himalaya regions, 2) discuss the spread among the various models and 3) highlight some of the factors responsible for the differences in model simulations and projections in the two domains of the HKKH region. For this study, we have employed two long observation-based precipitation datasets to evaluate/validate the model performances in the historical period. One is the Climate Research Unit (CRU) product, consisting of monthly gridded fields of precipitation from 1901 to 2009 over land areas; the other one is the recent Global Precipitation Climatology Centre (GPCC) full data reanalysis (GPCC FD), covering the time period from 1901 to 2010 and consisting of monthly precipitation data. We have adopted the same methodological approach as in Palazzi et al. (2013), by defining two sub-domains of the HKKH region, the HKK in the west (71°E - 78°E / 32°N - 37°N) and the Himalaya in the east (78°E - 93°E / 25°N - 32°N), and by evaluating the spatial-averages of precipitation (from the models and the two observation-based datasets) over the two sub-regions. In particular, the spatial averages over the two sub-regions have been performed by averaging the model pixels with their fraction of area with elevation higher than 1,000 m above mean sea level, determined using 2-Minute Gridded Global Relief Data (ETOPO2v2, <http://www.ngdc.noaa.gov/mgg/fliers/06mgg01.html>).

The employed CMIP5 models, their spatial resolution (longitude x latitude) and number of vertical levels in the atmosphere, the way they represent aerosol indirect effects and one key reference are shown in Table 1.1. For the details and model specifications we refer to the Program for Climate Model Diagnosis and Intercomparison (PCMDI) web page (<http://cmip-pcmdi.llnl.gov/cmip5/>). With respect to the previous generation of climate models (CMIP3), CMIP5 includes more and new GCMs with generally higher spatial resolution, an expanded variable list, a broader range of experiments and, in general, more Earth System Models (ESMs), including a representation of various biogeochemical cycles (Taylor et al, 2012). In comparison to the CMIP3 climate models, CMIP5 models generally have an improved representation of aerosol-cloud interactions (Wilcox et al, 2013) and most of them represent both the direct effect of sulphate aerosol and some of the indirect effects involving cloud droplet number and size. On short time-scales, the precipitation is strongly influenced by aerosol particles through indirect effects (Kaufman and Fraser, 1997). Among other studies, the work by Wilcox et al (2013) underlines the importance of representing aerosol indirect effects in the GCMs and suggests that the spread and diversity in the model simulations could be related to the different representation in aerosol burden and sensitivity of clouds to aerosols. In particular, anthropogenic aerosols in the monsoon regions are a possible driver for either weakening or strengthening of the monsoon circulation and for decreasing or increasing rainfall in the south-Asian monsoon region (Ramanathan et al, 2005; Lau et al, 2006).

In Table 1.1, we specify whether the employed CMIP5 models accounting for the indirect effects of sulphate aerosols do represent the first indirect effect only (the response of cloud droplet radius and cloud droplet number concentration to aerosol concentration) or both the first and second effects (the impact on cloud lifetime, depth, and liquid water

content). Compared to CMIP3, moreover, a higher number of CMIP5 ESMs includes an interactive representation of aerosol species (Wilcox et al, 2013): starred entries in Table 1.1 indicate the models with a fully interactive aerosol module.

Tab. 1.1: The CMIP5 models used in this study. Starred entries indicate models with a fully interactive aerosol module.

Model ID	Resolution Lon×Lat° Lev	Institution ID	First/second indirect aerosol effect	Key reference
bcc-csm1-1-m	1.125×1.125L26 (T106)	BCC	No	Wu et al (2013)
bcc-csm1-1	2.8125×2.8125L26 (T42)	BCC	No	Wu et al (2013)
CCSM4	1.25×0.9L27 (T63)	NCAR	No	Meehl et al (2012)
CESM1-BGC	1.25×0.9L27	NSF-DOE-NCAR	No	Hurrell et al (2013)
*CESM1-CAM5	1.25×0.9L27	NSF-DOE-NCAR	No	Hurrell et al (2013)
EC-Earth	1.125×1.125L62 (T159)	EC-EARTH	No	Hazeleger et al (2012)
FIO-ESM	2.8125×2.8125L26 (T42)	FIO	No	Song et al (2012)
GFDL-ESM2G	2.5×2L24 (M45)	GFDL	No	Delworth et al (2006)
GFDL-ESM2M	2.5×2L24 (M45)	GFDL	No	Delworth et al (2006)
MPI-ESM-LR	1.875×1.875L47 (T63)	MPI-M	No	Giorgetta et al (2013)
MPI-ESM-MR	1.875×1.875L95 (T63)	MPI-M	No	Giorgetta et al (2013)
*CanESM2	2.8125×2.8125L35 (T63)	CCCMA	Yes / No	Arora et al (2011)
CMCC-CMS	1.875×1.875L95 (T63)	CMCC	Yes / No	Davini et al (2013)
CNRM-CM5	1.40625×1.40625L31 (T127)	CNRM- CERFACS	Yes / No	Voltaire et al (2013)
*CSIRO-Mk3-6-0	1.875×1.875L18 (T63)	CSIRO- QCCCE	Yes / No	Rotstayn et al (2012)
*GFDL-CM3	2.5×2L48 (C48)	GFDL	Yes / No	Delworth et al (2006)
INM-CM4	2×1.5L21	INM	Yes / No	Volodin et al (2010)
IPSL-CM5A-LR	3.75×1.89L39	IPSL	Yes / No	Hourdin et al (2013)
IPSL-CM5A-MR	2.5×1.2587L39	IPSL	Yes / No	Hourdin et al (2013)
IPSL-CM5B-LR	3.75×1.9L39	IPSL	Yes / No	Hourdin et al (2013)
*MRI-CGCM3	1.125×1.125L48 (T159)	MRI	Yes / No	Yukimoto et al (2012)
CMCC-CM	0.75×0.75L31 (T159)	CMCC	Yes / N/A	Scoccimarro et al (2011)
FGOALS-g2	2.8125×2.8125L26	LASG-CESS	Yes / N/A	Li et al (2013)
*HadGEM2-AO	1.875×1.24L60	MOHC	Yes / N/A	Martin et al (2011)
*ACCESS1-0	1.875×1.25L38 (N96)	CSIRO-BOM	Yes / Yes	Bi et al (2013)
*ACCESS1-3	1.875×1.25L38	CSIRO-BOM	Yes / Yes	Bi et al (2013)
*HadGEM2-CC	1.875×1.24L60 (N96)	MOHC	Yes / Yes	Martin et al (2011)
*HadGEM2-ES	1.875×1.24L38 (N96)	MOHC	Yes / Yes	Bellouin et al (2011)
*MIROC5	1.40625×1.40625L40 (T85)	MIROC	Yes / Yes	Watanabe et al (2010)
*MIROC-ESM	2.8125×2.8125L80 (T42)	MIROC	Yes / Yes	Watanabe et al (2011)
*NorESM1-M	2.5×1.9L26 (F19)	NCC	Yes / Yes	Bentsen et al (2013)
*NorESM1-ME	2.5×1.9L26	NCC	Yes / Yes	Bentsen et al (2013)

We have first analysed the CMIP5 seasonal precipitation climatology in the Himalaya and HKK regions, looking at the mean annual cycle of precipitation, averaged over the historical period (1901-2005, Fig. 1.1a) and over the future decades (2600-2100, Fig. 1.1b). Each grey line indicates the output of an individual model, the multi-model mean (MMM) is shown with the black solid line, while CRU and GPCP observations are shown with the pink and green lines, respectively. With respect to CRU, the CMIP5 MMM indicates an overestimation of the simulated precipitation all over the year in both the HKK and Himalayan regions, a positive bias which is commonly found in the precipitation simulated by the state-of-the-art GCMs over high-elevated terrains, such as the Andes, Sierra Madre, and in the Tibetan Plateau (Lee et al, 2010). The same model bias is found with respect to GPCP data, except for July and August precipitation in the HKK region. As shown in Figs. 1.1a and 1.1b, the model spread relative to the multi-model mean is large in both sub-regions, indicating that the models do not converge in their representation of the historical precipitation annual cycle. On the other hand, remarkable differences between the two regions exist. All models, in fact, reproduce one-modal precipitation annual cycles in the Himalayan region, even if with different widths and different amplitudes, while the model disagreement is much more serious in the HKK region, where annual cycles with very different characteristics are clearly simulated. In

order to better understand how many different kinds of precipitation annual cycle in HKK are simulated by the CMIP5 models, we have applied a hierarchical clustering analysis, using a standard Euclidean distance as a distance metric, based on the features of the simulated precipitation annual cycle, so assuming no a priori knowledge about the model characteristics.

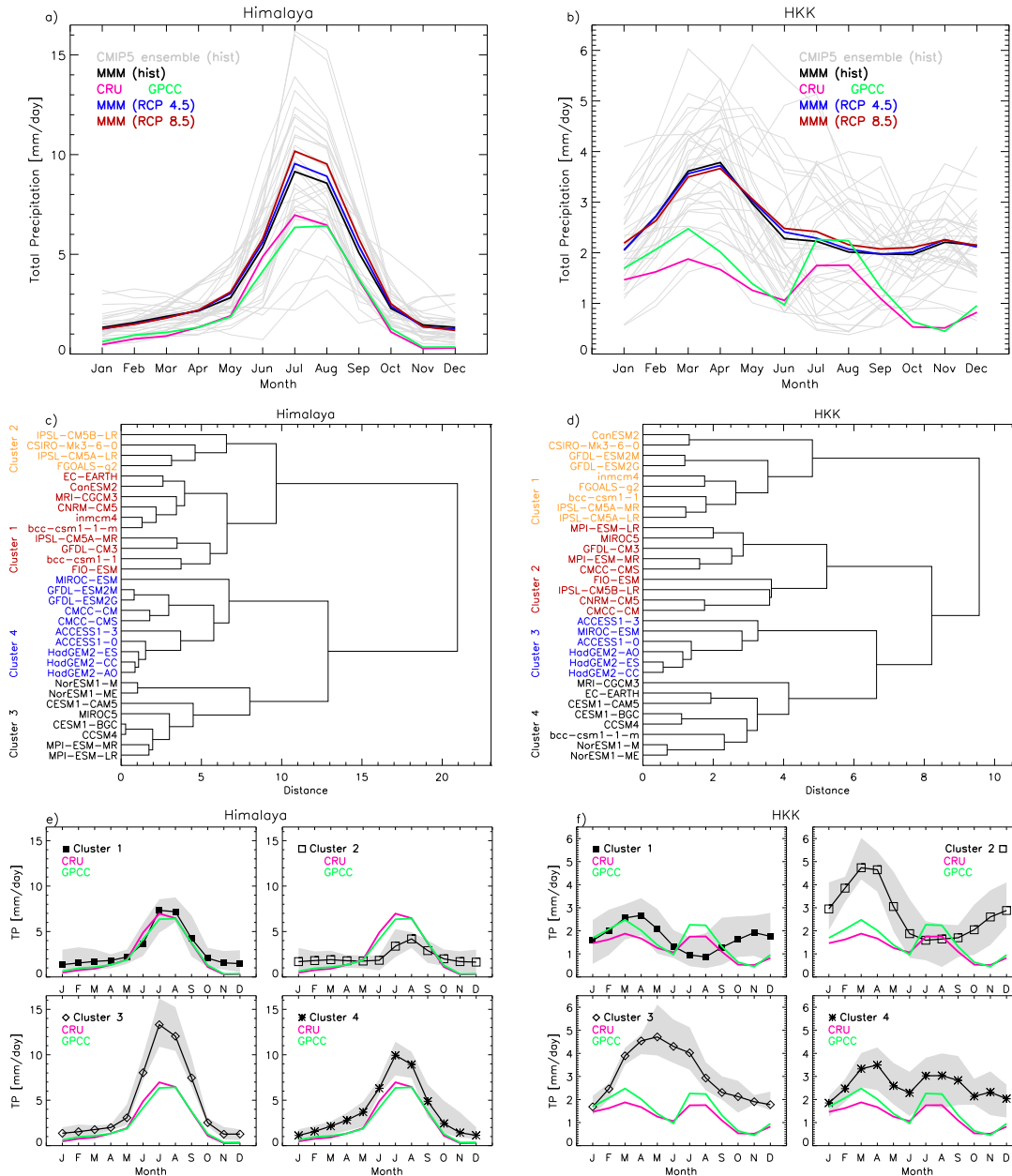


Fig. 1.1: Mean annual cycle of precipitation in the Himalaya (a) and HKK (b), obtained as a multi-annual average over the years 1901-2005 (historical period) for each CMIP5 model (grey lines) and for their multi-model mean (MMM, black line). The solid blue and red lines represent the mean annual cycle of precipitation over the years 2006-2100 in the RCP 4.5 and the RCP 8.5 future scenarios, respectively, for the CMIP5 MMM. Panels c) and d) show the dendrograms illustrating model clusters in the Himalaya and HKK regions, obtained by applying a hierarchical clustering analysis (four clusters are identified in each region). e) Mean annual cycle of precipitation in the Himalaya simulated by all models within each cluster (the grey shaded areas indicate the variability range of the models) and by their MMM. f) The same as panel e) for the HKK region. Panels a), b), e) and f) show the CRU and GPCC observations with the pink and green lines, respectively.

Four model clusters have been identified in the HKK region, as shown in the dendrogram plot of Fig. 1.1d. For each cluster, we show in the four panels of Figs. 1.1f the precipitation annual cycle simulated by the models in each cluster (shaded area) and by their mean (black solid lines with symbols), along with the CRU and GPCP observations. Models in the first and second clusters simulate very few amounts of precipitation during Summer compared to winter/early spring precipitation. The main difference between the two clusters is that the second one is on average characterized by larger precipitation amounts. The models in the third cluster display a wide precipitation distribution, with high precipitation values from March to August and one peak around May; precipitation values are strongly overestimated with respect to the CRU and GPCP observations. Finally, models in the fourth group present a simulated annual cycle most similar to the CRU and GPCP observations in which the yearly precipitation distribution exhibits two peaks, one in late winter/early spring and the other in summer. This seasonal distribution of precipitation has been described and discussed in Palazzi et al. (2013) and reflects the two main seasonal precipitation sources in the area, the wintertime western weather patterns and the summer monsoon. A third, lower, maximum in November can be mainly attributed to one single model, MRI-CGCM3. The mean annual distribution of precipitation reproduced by these models, however, exhibits a systematic wet bias relative to the observations. All models belonging to this cluster have a resolution of either 1.125° or 1.25° longitude (high-resolution models), except the NorESM family models, having a coarser resolution of 2.5° degrees longitude.

For completeness, we have applied the same clustering analysis to the Himalayan region (Figs. 1.1c and 1.1e): the results shown in the four sub-plots in Fig. 1.1e confirm that, for each model cluster, the average precipitation annual cycle in the Himalayan region is described by a one-modal distribution peaked in Summer. The amplitude of the peak varies across the clusters, the maximum of precipitation being in the range from 4 mm/day to 14 mm/day. In spite of the MMM wet bias discussed above, this further analysis indicates that some models do not overestimate the observed precipitation annual cycle in the Himalayan sub-region, but they either exhibit a dry bias relative to the observations (cluster 2), or are very close to the observations (cluster 1) in the summer months. Cluster 1 models, for example, have spatial resolutions ranging from 1.125° to 2.8125° longitude, and they either include the only direct or both the direct and indirect effects of sulphate aerosol (but none of them accounts for the second indirect aerosol effect). Therefore, neither the horizontal resolution, nor the representation of the indirect aerosol effects, seem to be decisive factors explaining the good agreement between the annual cycle simulated by models in this cluster and the observations. Models in cluster 2 display a precipitation annual cycle in the Himalayan region with a maximum shifted to August and with precipitation values largely underestimated in JJAS, compared to both observational datasets. As for the models in cluster 1, a wet bias from October to April is detected. The second cluster models have a coarser spatial resolution than models of cluster 1, ranging from 1.875° to 3.75° longitude. The models in the third and fourth clusters simulate similar annual distributions of precipitation. They both overestimate the observations all over the year and have a maximum in July, of about 13-14 mm/day (cluster 3) or 10 mm/day (cluster 4).

Panels a) and b) of Fig. 1.1 also show the mean precipitation annual cycle averaged over the years 2006-2100 in the RCP 4.5 and RCP 8.5 scenarios with the blue and red lines, respectively, obtained by averaging all CMIP5 models. The CMIP5 MMM indicates higher precipitation in the future with respect to the historical precipitation average, from about

May to October in the Himalayan region, with higher values for the RCP 8.5 than for the RCP 4.5 scenario, especially in the warmest months. In the HKK region from about February to May, future precipitation appears to be close to or slightly lower than the present-day value in both scenarios, while from about May to November future precipitation is slightly higher than the historical one, particularly in the RCP 8.5 scenario.

To better analyse the inter-model differences and their biases with respect to the observations in the historical period, we report in Tables 1.2 (for the Himalaya) and Table 1.3 (HKK) the average summer and winter precipitation values in the baseline period (1901-2005) for all CMIP5 models, for their MMM and for the CRU and GPCC observations, together with the precipitation bias between the individual models, their mean, and GPCC relative to CRU.

Tab. 1.2: Average summer and winter precipitation over the baseline historical period 1901- 2005, in Himalaya, for each CMIP5 model, for the MMM, and for the CRU and GPCC observations. The table also shows the precipitation bias, relative to CRU, of all GCMs, of the MMM and of the GPCC data. A negative bias is highlighted in italic. Starred entries indicate models with a fully interactive aerosol module; bold style is used to indicate the models representing the indirect aerosol effect.

Model	Mean JJAS Precip. [mm day ⁻¹]	JJAS Bias Data-CRU [%]	Mean DJFMA Precip. [mm day ⁻¹]	DJFMA Bias Data-CRU [%]
bcc-csm1-1-m	5.67	0.16	1.63	0.88
bcc-csm1-1	4.91	<i>-0.59</i>	2.49	1.73
CCSM4	9.36	3.85	1.39	0.64
CESM1-BGC	9.46	3.95	1.38	0.62
*CESM1-CAM5	10.65	5.15	1.02	0.26
EC-Earth	5.71	0.21	0.99	0.23
FIO-ESM	6.21	0.70	2.87	2.12
GFDL-ESM2G	8.08	2.57	1.10	0.34
GFDL-ESM2M	8.14	2.63	1.14	0.39
MPI-ESM-LR	9.95	4.44	1.55	0.79
MPI-ESM-MR	9.36	3.85	1.78	1.02
*CanESM2	5.25	<i>-0.26</i>	0.72	<i>-0.03</i>
CMCC-CMS	7.75	2.24	2.16	1.40
CNRM-CM5	6.09	0.58	1.75	1.00
*CSIRO-Mk3-6-0	3.84	<i>-1.66</i>	0.79	0.04
*GFDL-CM3	6.50	0.99	1.56	0.81
INM-CM4	5.36	<i>-0.15</i>	1.50	0.75
IPSL-CM5A-LR	3.07	<i>-2.44</i>	1.77	1.02
IPSL-CM5A-MR	5.03	<i>-0.47</i>	1.25	0.50
IPSL-CM5B-LR	2.31	<i>-3.19</i>	2.84	2.08
*MRI-CGCM3	5.26	<i>-0.25</i>	1.01	0.25
CMCC-CM	8.19	2.69	1.70	0.94
FGOALS-g2	3.08	<i>-2.42</i>	1.66	0.90
*HadGEM2-AO	7.15	1.65	1.82	1.07
*ACCESS1-0	6.53	1.02	1.87	1.12
*ACCESS1-3	8.06	2.55	2.01	1.26
*HadGEM2-CC	7.14	1.63	1.90	1.15
*HadGEM2-ES	6.75	1.25	1.80	1.05
*MIROC5	8.95	3.44	1.61	0.86
*MIROC-ESM	7.37	1.86	2.02	1.27
*NorESM1-M	11.87	6.36	2.00	1.24
*NorESM1-ME	12.11	6.60	1.98	1.23
MMM	7.04	1.53	1.66	0.90
GPCC	5.17	<i>-0.33</i>	0.87	0.12
CRU	5.51	-	0.75	-

As already noted in the discussion of the precipitation annual cycle, the MMM displays a positive precipitation bias relative to CRU in the period 1901-2005, in both regions and seasons. Similar positive biases are found relative to GPCC (not shown). This confirms the

results of previous model assessment studies (Solomon et al, 2007) discussing the overall skill of the models in simulating current precipitation in the South-East Asia and in Tibetan Plateau sub-continental regions. Looking at the individual model biases, we see that, for both regions, both positive and negative biases are associated with summer precipitation, while precipitation biases are largely positive in winter. In fact, during winter, only one model (CanESM2) displays a small negative bias with relative to CRU in the Himalayan region, and two models (CanESM2 and CSIRO-Mk3-6-0) are on average drier than the CRU observations in the HKK region. The reasons for the general positive precipitation bias found in winter could be attributed either to the model inaccuracies in representing small-scale processes, mainly due to the models coarse spatial resolution (Lee et al, 2010), or to a shortcoming of station and gridded data which tend to neglect the snow component of precipitation (Rasmussen et al, 2012), or to a combination of both aspects.

Tab. 1.3: The same as Table 1.2, but for the HKK

Model	Mean JJAS Precip. [mm day ⁻¹]	JJAS Bias Data-CRU [%]	Mean DJFMA Precip. [mm day ⁻¹]	DJFMA Bias Data-CRU [%]
bcc-csm1-1-m	3.12	1.70	2.43	0.93
bcc-csm1-1	0.59	-0.82	2.25	0.75
CCSM4	3.52	2.11	3.01	1.52
CESM1-BGC	3.18	1.76	3.01	1.52
*CESM1-CAM5	2.51	1.09	2.53	1.03
EC-Earth	3.08	1.66	2.14	0.65
FIO-ESM	1.40	-0.02	4.11	2.61
GFDL-ESM2G	1.75	0.34	2.08	0.58
GFDL-ESM2M	1.68	0.27	1.84	0.34
MPI-ESM-LR	2.03	0.62	3.41	1.91
MPI-ESM-MR	1.98	0.56	4.00	2.51
*CanESM2	0.90	-0.52	1.13	-0.37
CMCC-CMS	1.34	-0.0	3.93	2.43
CNRM-CM5	2.13	0.72	3.84	2.34
*CSIRO-Mk3-6-0	0.69	-0.73	1.28	-0.22
*GFDL-CM3	1.71	0.30	3.14	1.64
INM-CM4	1.41	-0.01	2.72	1.22
IPSL-CM5A-LR	0.83	-0.51	2.89	1.40
IPSL-CM5A-MR	0.92	-0.50	2.53	1.04
IPSL-CM5B-LR	1.38	-0.04	3.40	2.50
*MRI-CGCM3	2.09	0.67	2.67	1.17
CMCC-CM	2.20	0.78	4.46	2.97
FGOALS-g2	1.21	-0.20	2.35	0.85
*HadGEM2-AO	3.01	1.59	2.76	1.26
*ACCESS1-0	2.98	1.57	2.73	1.23
*ACCESS1-3	4.05	2.64	2.72	1.22
*HadGEM2-CC	3.22	1.81	3.01	1.52
*HadGEM2-ES	3.00	1.58	2.96	1.46
*MIROC5	1.15	-0.26	3.43	1.93
*MIROC-ESM	4.08	2.67	3.04	1.55
*NorESM1-M	2.45	1.04	2.63	1.13
*NorESM1-ME	2.42	1.01	2.65	1.16
MMM	2.13	0.71	2.87	1.37
GPCC	1.70	0.28	1.84	0.35
CRU	1.41	-	1.50	-

Figure 1.2 shows the seasonal time series of the precipitation anomalies from 1870 to 2100 in the Himalayan and HKK regions. The anomaly is evaluated relative to the average precipitation in the baseline period (1901-2005), as shown in Tables 1.2 and 1.3.

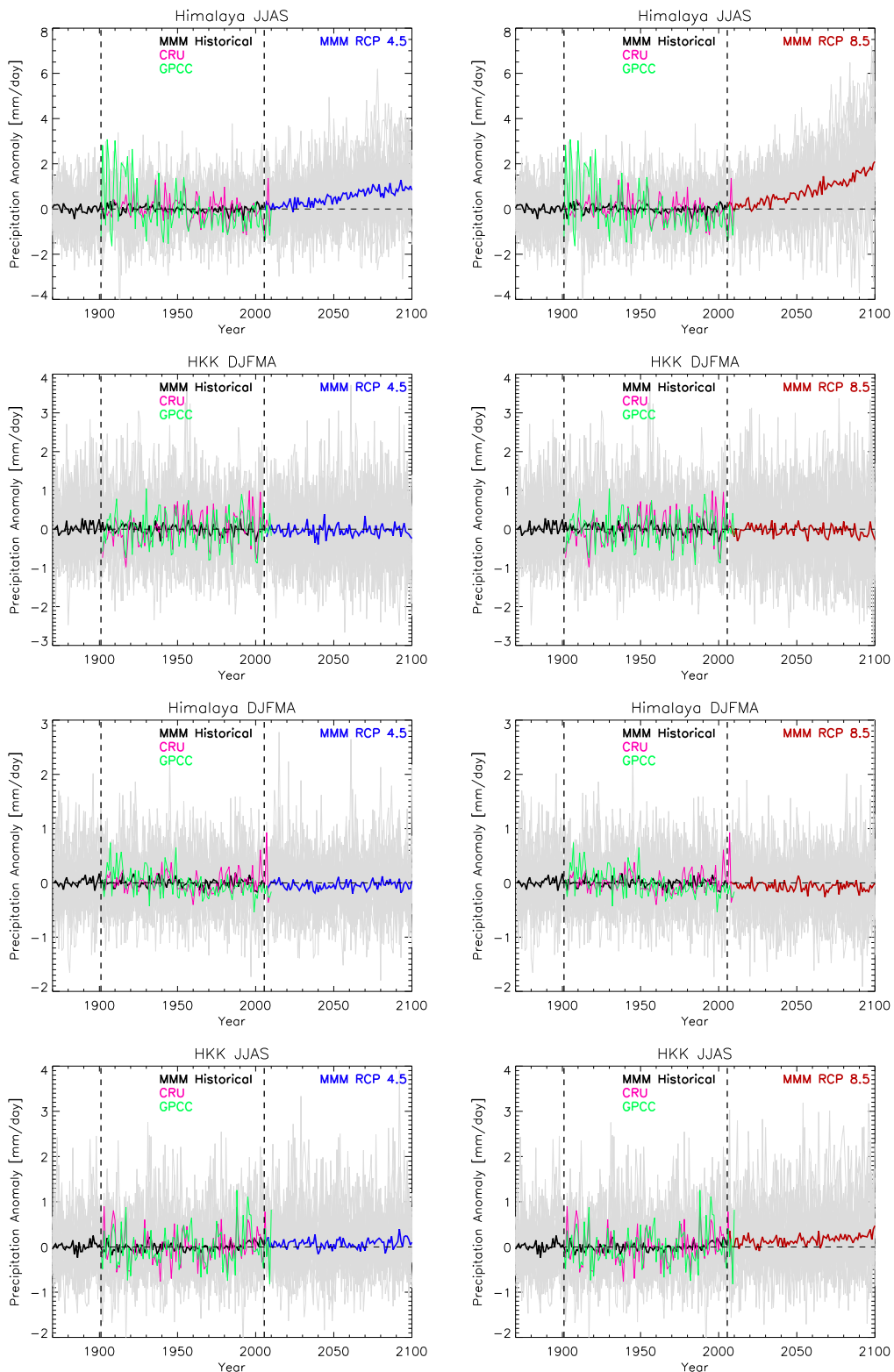


Fig. 1.2: Time series of precipitation anomalies in the Himalaya and in the HKK during Summer and Winter from 1870 to 2005 and from 2600 to 2100 (RCP 4.5, left column; RCP 8.5, right column). The individual models of the CMIP5 ensemble are shown in grey, the CMIP5 multi-model mean (MMM) is shown with the black (historical period), blue (RCP 4.5 scenario) and red (RCP 8.5 scenario) solid lines. CRU and GPCP observations are shown with the pink and green lines, respectively. The anomalies are evaluated with respect to the 1901-2005 baseline period.

The individual GCM outputs are shown with the grey lines, the multi-model mean (MMM) with the black solid line (historical period), and with blue (RCP 4.5) and red (RCP 8.5) lines. The CRU and GPCP precipitation anomalies are shown with the pink and green lines, respectively. The historical and future trends of summer and winter precipitation (in mm/day per century) for the models and the CRU and GPCP observations are shown in Tables 1.4 (Himalaya) and 1.5 (HKK).

Tab. 1.4: Trends (in mm/day/century) in the Himalaya during JJAS and DJFMA, in the periods 1901-2005 and 2006-2100 (RCP4.5 and RCP8.5 scenarios) for the CMIP5 models and for the MMM. Historical precipitation trends for the CRU and GPCP datasets are also indicated. Statistically significant trends are highlighted in bold. Starred entries indicate models with a fully interactive aerosol module; bold entries indicate models representing the indirect aerosol effect.

	JJAS			DJFMA		
	Historical 1901-2005	RCP4.5 2006-2100	RCP8.5 2006-2100	Historical 1901-2005	RCP4.5 2006-2100	RCP8.5 2006-2100
Observations						
CRU	-0.369			0.048		
GPCP	-1.445			-0.355		
CMIP5 models						
bcc-csm1-1-m	0.010	0.171	0.827	0.170	-0.131	-0.066
bcc-csm1-1	0.026	0.847	2.076	-0.015	0.391	0.797
CCSM4	0.283	0.507	1.746	-0.123	-0.084	-0.127
CESM1-BGC	-0.114	0.837	1.866	-0.042	-0.088	-0.193
*CESM1-CAM5	-0.395	2.588	3.806	0.020	0.033	0.135
EC-Earth	0.516	0.003	1.082	0.101	0.162	0.097
FIO-ESM	0.042	-1.547	-0.828	0.000	-0.099	-0.328
GFDL-ESM2G	0.164	0.711	4.198	0.101	-0.040	0.242
GFDL-ESM2M	-0.014	1.445	2.534	0.127	0.140	0.299
MPI-ESM-LR	-0.114	-0.356	0.183	-0.082	-0.188	-0.233
MPI-ESM-MR	0.464	0.153	-0.011	-0.262	-0.044	-0.483
*CanESM2	-1.009	1.553	2.214	0.003	-0.012	0.331
CMCC-CMS	0.136	0.610	-0.035	0.047	-0.484	-0.460
CNRM-CM5	0.194	0.567	1.769	0.034	0.238	0.462
*CSIRO-Mk3-6-0	-0.079	0.162	0.785	-0.084	0.165	0.129
*GFDL-CM3	-0.799	4.873	6.583	0.134	0.022	-0.182
INM-CM4	0.073	0.758	1.874	-0.036	0.054	-0.238
IPSL-CM5A-LR	-0.088	0.860	1.021	-0.215	0.135	-0.641
IPSL-CM5A-MR	0.039	1.498	2.603	-0.031	0.069	-0.310
IPSL-CM5B-LR	-0.133	1.042	1.602	-0.012	0.172	0.315
*MRI-CGCM3	0.031	-0.265	0.330	-0.123	-0.022	0.215
CMCC-CM	-0.161	0.239	0.956	0.161	-0.212	-0.524
FGOALS-g2	0.313	0.914	2.215	0.190	-0.261	-0.351
*HadGEM2-AO	-0.436	1.228	1.129	-0.150	0.061	-0.051
*ACCESS1-0	-0.476	0.699	1.150	-0.105	-0.063	-0.183
*ACCESS1-3	-0.537	1.953	2.996	0.076	-0.017	-0.071
*HadGEM2-CC	-0.746	1.662	1.507	-0.086	0.227	-0.076
*HadGEM2-ES	-0.445	1.356	1.295	-0.189	0.012	-0.091
*MIROC5	0.585	2.210	3.769	-0.064	0.062	0.292
*MIROC-ESM	0.358	1.620	2.432	-0.239	0.266	-0.036
*NorESM1-M	-0.045	1.838	2.469	0.103	0.053	-0.110
*NorESM1-ME	-0.075	1.976	2.295	0.230	-0.017	-0.182
MMM	-0.076	1.127	1.860	-0.011	0.016	-0.051

For the Himalayan region, we see that only seven GCMs (CanESM2, GFDL-CM3, HadGEM-AO, ACCESS-0-1, ACCESS-0-3, HadGEM-CC, and HadGEM-ES) simulate, in agreement with the two observational datasets, a statistically significant decreasing trend during Summer in the period 1901-2005; for all of them, however, the trends are stronger (weaker) than the one inferred from CRU (GPCP) data. Five of these models (the HadGEM2- and ACCESS- family ESMs) share the same lineage. The seven GCMs listed above do not have particularly high horizontal resolution (from 1.875 to 2.8125° longitude) but they do account for the first and second indirect effect of sulphate aerosols. Three models (EC-

Earth, FGOALS-g2, and MIROC5), on the other hand, simulate statistically significant trends of opposite sign for the historical period in this region and season.

Tab. 1.5: As in Table 1.4, but for the HKK region.

	JJAS			DJFMA		
	Historical 1901-2005	RCP4.5 2006-2100	RCP8.5 2006-2100	Historical 1901-2005	RCP4.5 2006-2100	RCP8.5 2006-2100
Observations						
CRU	0.083			0.399		
GPCC	0.101			0.002		
CMIP5 models						
bcc-csm1-1-m	0.544	0.596	0.493	-0.091	0.126	-0.078
bcc-csm1-1	-0.061	0.158	0.054	-0.238	-0.198	0.011
CCSM4	-0.019	0.004	0.255	-0.264	-0.089	-0.292
CESM1-BGC	-0.352	0.522	-0.193	-0.271	-0.117	-0.529
*CESM1-CAM5	0.550	-0.739	0.054	-0.045	-0.058	0.226
EC-Earth	0.186	0.023	0.033	-0.013	0.458	0.344
FIO-ESM	0.335	0.116	0.184	-0.228	-0.506	-1.141
GFDL-ESM2G	-0.003	0.297	0.674	0.159	-0.070	0.025
GFDL-ESM2M	0.628	0.254	0.613	0.017	-0.126	0.044
MPI-ESM-LR	-0.013	-0.064	-0.258	-0.510	-0.528	-1.140
MPI-ESM-MR	-0.052	0.173	0.005	-0.286	0.199	-1.010
*CanESM2	0.030	-0.104	0.011	0.000	-0.114	0.181
CMCC-CMS	0.261	-0.013	-0.129	-0.194	-0.871	-0.840
CNRM-CM5	0.040	-0.102	0.338	0.339	0.160	0.989
*CSIRO-Mk3-6-0	0.079	0.143	-0.054	-0.242	0.378	0.554
*GFDL-CM3	-0.071	0.334	0.296	0.039	-0.066	-0.398
INM-CM4	0.044	0.052	0.196	-0.178	-0.098	-0.591
IPSL-CM5A-LR	-0.009	-0.287	-0.120	-0.250	0.426	-0.600
IPSL-CM5A-MR	0.188	0.065	0.300	-0.373	0.469	-0.234
IPSL-CM5B-LR	-0.015	0.151	0.633	-0.106	0.476	0.736
*MRI-CGCM3	0.462	-0.214	0.470	0.014	0.275	1.117
CMCC-CM	0.147	-0.045	0.073	-0.163	0.332	0.305
FGOALS-g2	0.055	-0.204	0.192	0.185	-0.578	-0.608
*HadGEM2-AO	0.003	0.206	0.044	-0.128	0.254	0.418
*ACCESS1-0	-0.133	-0.423	-0.196	0.181	0.013	0.167
*ACCESS1-3	0.062	-0.276	-0.351	0.142	0.085	0.300
*HadGEM2-CC	-0.243	0.189	0.142	-0.099	0.345	0.187
*HadGEM2-ES	-0.206	0.271	0.265	-0.046	-0.009	0.242
*MIROC5	0.300	0.238	1.100	-0.037	-0.017	-0.248
*MIROC-ESM	-0.160	-0.216	0.002	0.019	-0.166	-0.598
*NorESM1-M	-0.115	0.290	0.412	0.023	-0.131	-0.105
*NorESM1-ME	0.534	0.281	0.425	0.308	-0.452	-0.530
MMM	0.094	0.054	0.186	-0.073	-0.006	-0.097

It is interesting to observe that, regardless of the model picture of the historical precipitation trends, almost all GCMs simulate increasing summer precipitation trends in the Himalaya up to 2100 in both emission scenarios, and in most cases these trends are statistically significant (particularly for the RCP 8.5 scenario). The multi-model mean shows, for the Himalaya in Summer, insignificant decreasing precipitation trends in the historical period, while statistically significant increasing trends in 2006-2100 of about 1.13 mm/day per century (RCP 4.5) and 1.86 mm/day per century (RCP 8.5). The Himalayan region is therefore expected to experience a future, and overall significant, increase in total precipitation amounts during the monsoon season, as a consequence of future warming driven by the increase of greenhouse gas emissions and concentrations and of the related intensification of the hydrological cycle (Trenberth et al, 2003).

In the Himalaya, during Winter, the MMM does not indicate significant precipitation trends in both the historical and future decades. About half of the models show negative trends of precipitation in the historical period, the other half shows positive, increasing precipitation trends. On the other hand, only two models (HadGEM2-AO, HadGEM2-ES),

belonging to the same family, give a statistically significant trend, indicating a decrease of total precipitation at a rate of about -0.2 mm/day per century in the period 1901-2005. It is worth pointing out, however, that the two observational datasets give different pictures of the historical winter precipitation trend in the Himalayan region: CRU data show a slight, positive and insignificant trend, while GPCC shows a negative, statistically significant precipitation trend (-0.355 mm/day per century). Future projections of winter precipitation in the Himalayan region are much less clear than the summer ones. In the RCP 8.5 scenario, we find a very slight prevalence of models giving statistically significant decreasing precipitation trends, but no conclusive considerations can be drawn from our analysis.

In the HKK region (Table 1.5), both observational datasets indicate positive, though insignificant, precipitation trends in Summer in the period 1901-2005. The MMM indicates a significant positive trend in this region and season, probably due to the significant positive trends, in the range from 0.3 to ~ 0.6 mm/day per century, simulated by five models. Future precipitation projections in the HKK region in summer indicate, on average (MMM), a positive trend in both scenarios, statistically significant only in the RCP 8.5 hypothesis. Looking at the results of the individual models displaying statistically significant trends, it is interesting to note that, while in the RCP 4.5 scenario both positive and negative trends are simulated, in the RCP 8.5 scenario the statistically significant trends are all positive, indicating that, in this scenario, not only the Himalayan region, but also the HKK is expected to experience a future increase in summer precipitation. In the HKK region in Winter, the MMM indicates negative precipitation trends throughout the historical period and the future decades. Historical trends are statistically significant, as are future precipitation trends under the RCP 8.5 scenario.

We conclude our analysis by discussing more in detail the seasonal precipitation changes between future decades and the historical period. For the analysis of the precipitation change, we choose 1971-2000 as the present-day reference period and 2021-2050 and 2071-2100 as future reference periods. In Figs. 1.3 and 1.4 we show the seasonal-mean percentage precipitation change in 2021-2050 relative to 1971-2000 (left column) and in 2071-2100 relative to 1971-2000 (right column) simulated by each CMIP5 GCM in the Himalaya and HKK regions, respectively. Results obtained in the RCP 4.5 (RCP 8.5) scenario are shown with the grey (black) histograms: filled histograms are used for the models giving statistically significant differences between future and historical average conditions.

Twenty out of thirty-two models display statistically significant precipitation changes in 2021-2050 relative to 1971-2000 in the Himalaya during summer (top left panel of Fig. 1.3), either in the RCP 4.5 or RCP 8.5 scenario or (mostly) in both scenarios. For all these models (except HadGEM2-AO in the RCP 4.5 scenario) the simulated change is positive, indicating that the GCMs simulate a wetter future in this region and season. Positive and statistically significant precipitation changes (ranging from less than $\sim 10\%$ to $\sim 80\%$ in the RCP 8.5 scenario) are also found in 2071-2100 relative to 1971-2000 for almost all models: only three GCMs (CMCC-CMS, MPI-ESM-LR, MPI-ESM-MR), built on the same atmospheric model, provide insignificant positive precipitation changes, while only one model (FIO-ESM) simulates significantly drier future conditions. Therefore, the CMIP5 models overall simulate a gradual increase of JJAS precipitation in the Himalaya throughout the twenty-first century, giving rise to positive precipitation changes both in the near and in the far future with respect to the historical (1971-2000) precipitation. A less clear signal emerges for winter precipitation changes in the Himalaya. Only five

models simulate statistically significant negative changes in 2021-2050 relative to 1971-2000, either in the RCP 4.5 and RCP 8.5 scenarios, while one model gives a positive, significant change. The number of GCMs simulating either positive or negative significant changes increases when the precipitation changes are evaluated in 2071-2100 relative to 1971-2000, with a slight prevalence towards a drier future under the RCP 8.5 scenario.

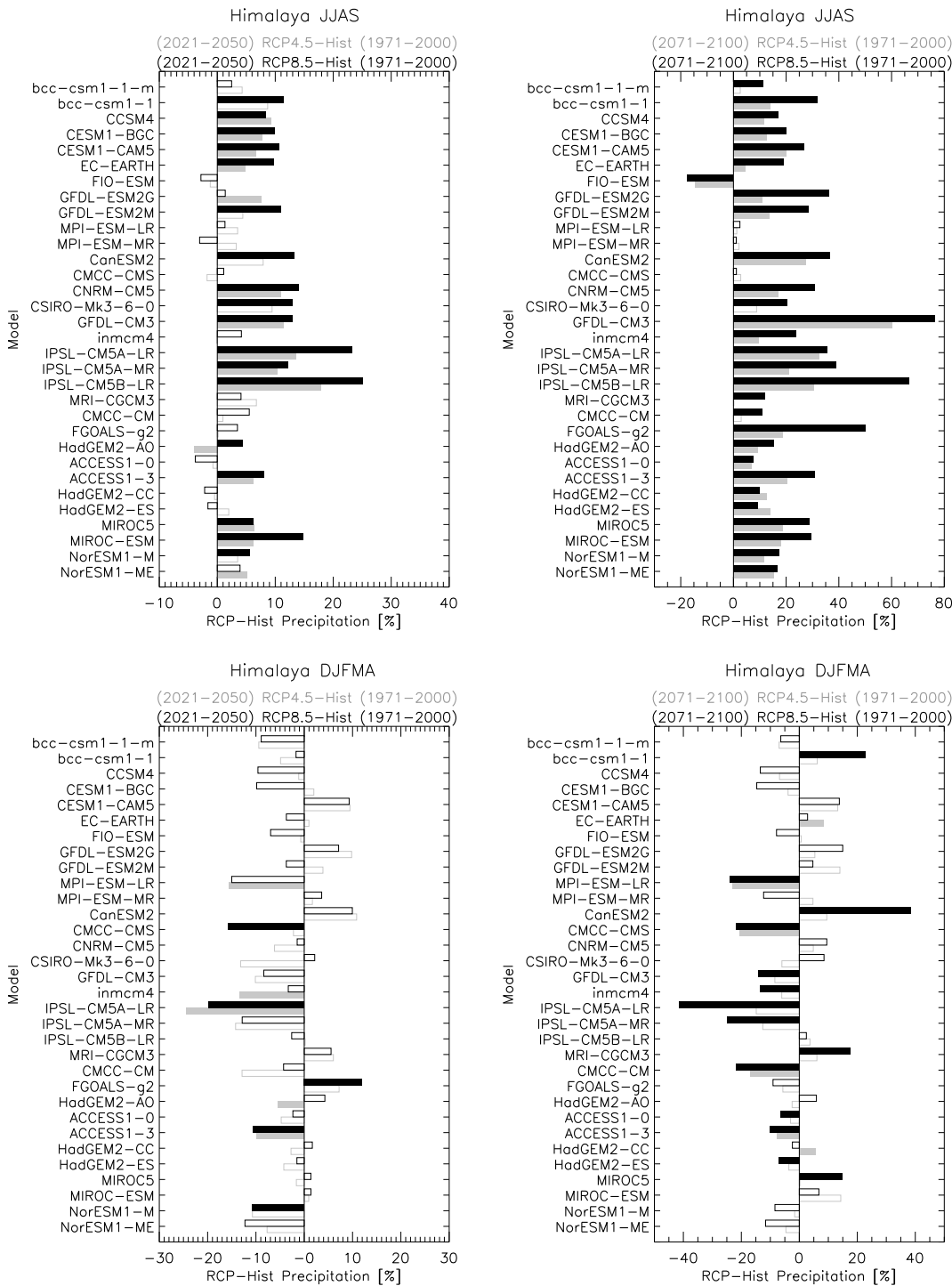


Fig. 1.3: Percentage change in summer (top) and winter (bottom) precipitation in the Himalaya in 2021-2050 (left column) or in 2071-2100 (right column) relative to 1971-2000. For the models displaying statistically significant precipitation changes we use filled histogram.

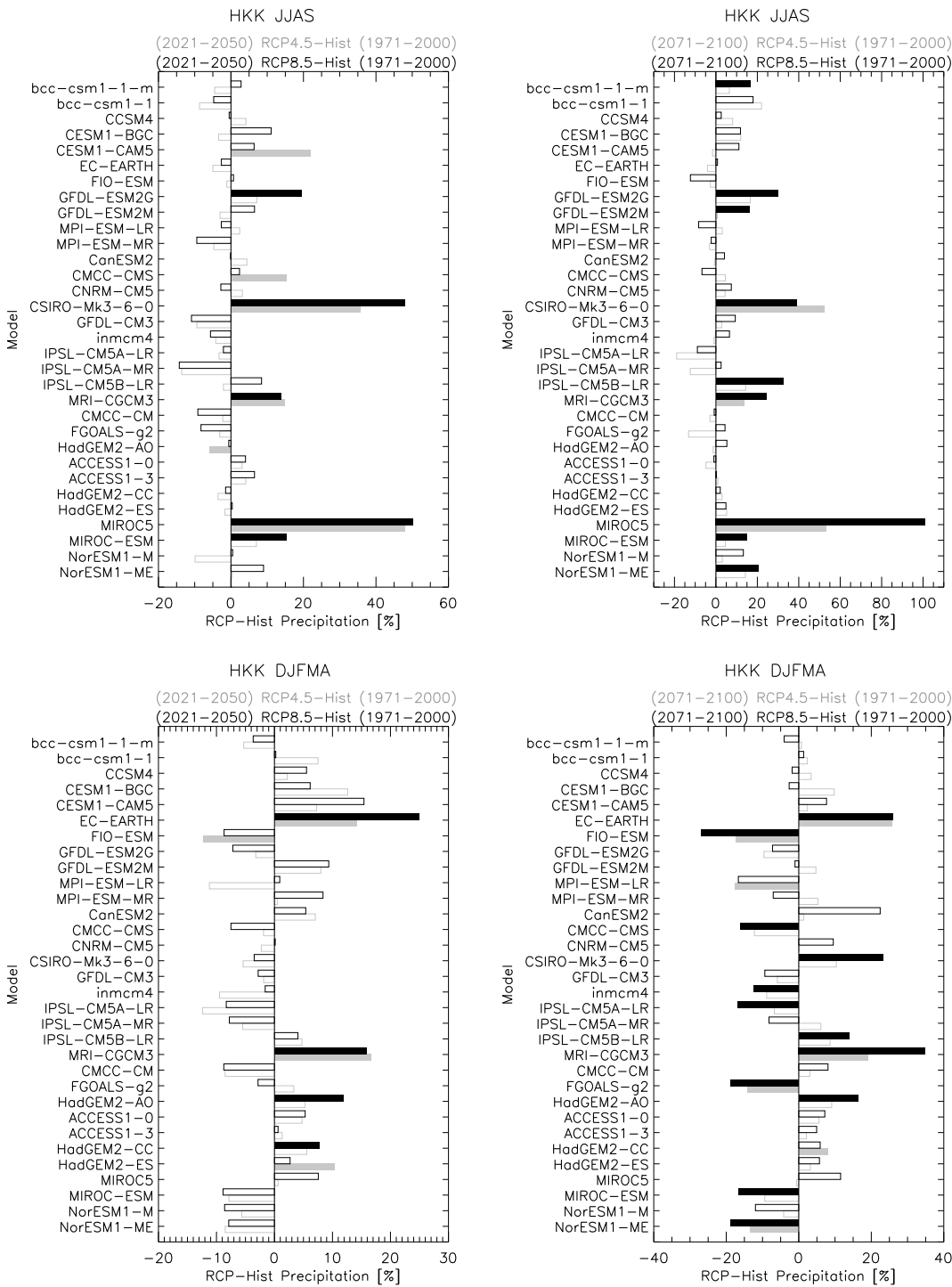


Fig. 1.4: As in Fig. 1.3, but for the HKK region.

The model picture of precipitation change in the HKK region indicates wetter conditions in Summer in both 2021-2050 and 2071-2100, relative to 1971-2000, as well as positive winter precipitation changes in the nearest future. However, it is worth pointing out that only a few models simulate statistically significant changes. The modelled winter precipitation change in 2071-2100 relative to 1971-2000 in the HKK is not homogeneous: a few models show significant wetter future conditions, a few others simulate a drier future (especially under the RCP 8.5 scenario). Overall, with respect to the Himalaya region, in the HKK a larger number of GCMs simulate no significant seasonal precipitation changes.

2. Synoptic control of winter precipitation in the Karakoram

The Hindu-Kush Karakoram, at the western edge of the whole Himalayan range, is strongly affected by westerly perturbations (WWPs) originating from the Mediterranean/Atlantic regions during Winter/early Spring and it is affected, at least in part, by the monsoon during Summer. As a result, precipitation in the HKK is characterized by a bimodal annual cycle as shown in various observation-based and reanalysis precipitation data (Palazzi et al., 2013). WWPs are primarily responsible for the build-up of seasonal snow cover over western Himalaya and the Karakoram, constituting an essential water reserve and a significant water source for several river basins (Archer and Fowler 2004).

The North Atlantic Oscillation (NAO) strongly affects the climate of the North Atlantic and European sectors during Winter (Hurrell et al., 2003), and it has been indicated as an important regulating factor also in the Karakoram region (Syed et al. 2006; Yadav et al., 2009). Studies on the NAO effects on winter precipitation can be found in the literature, showing that winter precipitation and the NAO are correlated with above (below) than normal precipitation over the HKK area during the positive (negative) NAO phase. Syed et al. (2010), in particular, observed an increase in the number and intensity of eastern Mediterranean storms reaching northern Pakistan during the positive NAO phase, as an effect of the enhanced sea level pressure and 500 hPa trough which develops over central-south western Asia in that phase. They also noticed that the transport of extra moisture during the positive NAO phase from the Mediterranean, the Caspian and the Arabian Sea contributes to the NAO-precipitation signal in northern Pakistan.

The second year activities of the pilot study has led to the identification of the processes responsible for the correlation between the NAO and winter precipitation in HKK. We have analysed how the NAO affects evaporation from the main moisture reservoirs and we have explored the mechanisms of moisture transport from these sources to the Karakoram region. To this purpose, we have used an ensemble of observation-based precipitation datasets, including three gridded archives based on the interpolation of in-situ rain gauge measurements (GPCC, CRU and APHRODITE) and TRMM satellite observations. We also analysed the following ERA40 variables: precipitation, evaporation and sea surface temperature, the horizontal wind components, specific humidity and 10m wind speeds. Since precipitation and evaporation are not assimilated in the reanalysis system but are produced by the forecast model, they may be susceptible to systematic model errors. For further details on the observation-based datasets employed in this study we refer to Palazzi et al. (2013).

We have defined the winter season as the period from December to March (DJFM), consistent with other studies analysing the relationships between teleconnection patterns and precipitation in this area (e.g., Syed et al. 2006, 2010; Yadav et al., 2009). We have adopted the DJFM station-based NAO index (NAOI), available at <http://goo.gl/opvFM>.

Winter precipitation in the HKK is associated with the arrival of westerly perturbations (WWPs) originating from the Atlantic and the Mediterranean region. The space-time propagation of these systems is illustrated in Fig. 2.1, showing the meridionally-averaged daily precipitation for one winter season (the year 2001 is taken as an example) for TRMM (left) and ERA40 (right), plotted as a function of longitude and time. Precipitation is averaged over the latitude band from 30°N to 45°N, while longitude

ranges from the Mediterranean basin to the HKK region, as shown in the top panels of the figure. Western weather patterns appear as intermittent rainy systems propagating eastward (middle panels), with alternating intensified and weakened precipitation, with a marked association with orographic features (see, for example, the intensified precipitation at about 50°E and 75°E, corresponding to the mountain regions of western Iran and the HKK, respectively). Figure 2.1 shows that the number of systems reaching the longitudes corresponding to the HKK region is higher during February-March than December-January and, as a consequence, conspicuous precipitation amounts in this area occur during late winter (see, for example, Palazzi et al., 2013).

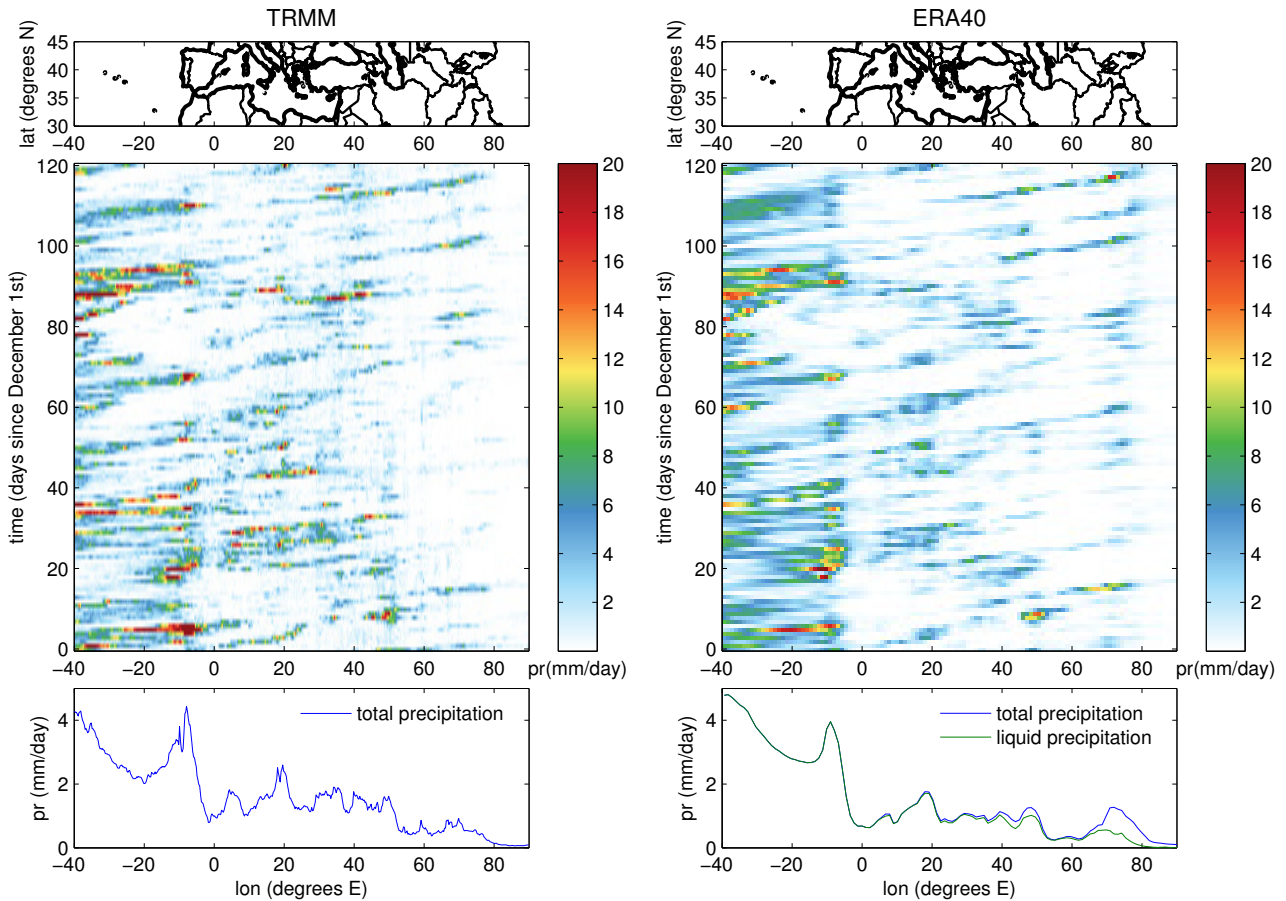


Fig. 2.1: Top: Maps showing the region considered in the analysis. Center: Daily precipitation in Winter 2001, from TRMM (left) and ERA40 (right) averaged over the latitudes from 30 to 45°N, plotted as a function of longitude and time. Bottom: Mean daily precipitation in Winter 2001, averaged over latitudes from 30 to 45°N.

As shown in Fig. 2.1, the main features of WWP tracks are qualitatively captured by precipitation from TRMM and ERA40. The two datasets provide a similar longitudinal distribution of mean precipitation, as shown by the bottom panels. TRMM shows slightly lower precipitation values over the Atlantic and higher values over the Mediterranean and the Middle East (up to about 50°E), while ERA40 shows a peak in total precipitation at HKK longitudes, between about 70°E and 80°E. This enhanced precipitation is not visible in the TRMM data, probably owing to the fact that the snow component of precipitation is neglected in the satellite estimates. The liquid-only precipitation in ERA40, shown as the green line in the bottom-right panel of Fig. 2.1, is much closer to the satellite-derived precipitation values.

As found in the literature, strong positive NAO phases tend to be associated with above-average precipitation over northern Europe in Winter, and below-average precipitation over southern and central Europe, while opposite patterns of precipitation anomalies are observed during strong negative NAO phases. This is the well known European precipitation dipole, the strongest signal emerging from Fig. 2.2, where the spatial distribution of the statistically significant correlations (at the 95% confidence level) between the DJFM precipitation and DJFM NAOI time series for the CRU, GPCC, APHRODITE and ERA40 datasets are displayed. Figure 2.2 shows that, beside the European sector, another area displaying statistically significant positive correlations in all datasets, though with some differences in spatial extent, is located at the border between north-eastern Pakistan and north-western India. Compared to the observation-based datasets, ERA40 shows significant positive correlations over a broader area encompassing central and northern Afghanistan and Pakistan, and the greater Himalayan chain. The correlation between liquid-only precipitation in ERA40 and the NAO (not shown here) is weaker than that calculated using total precipitation and is more similar, though still higher, to that inferred from the other datasets. Once again, this could be a signature of the underestimation of total precipitation in the observations, leading to an underestimation of the significance of the NAO-precipitation correlation signal when using datasets based on gridded observations.

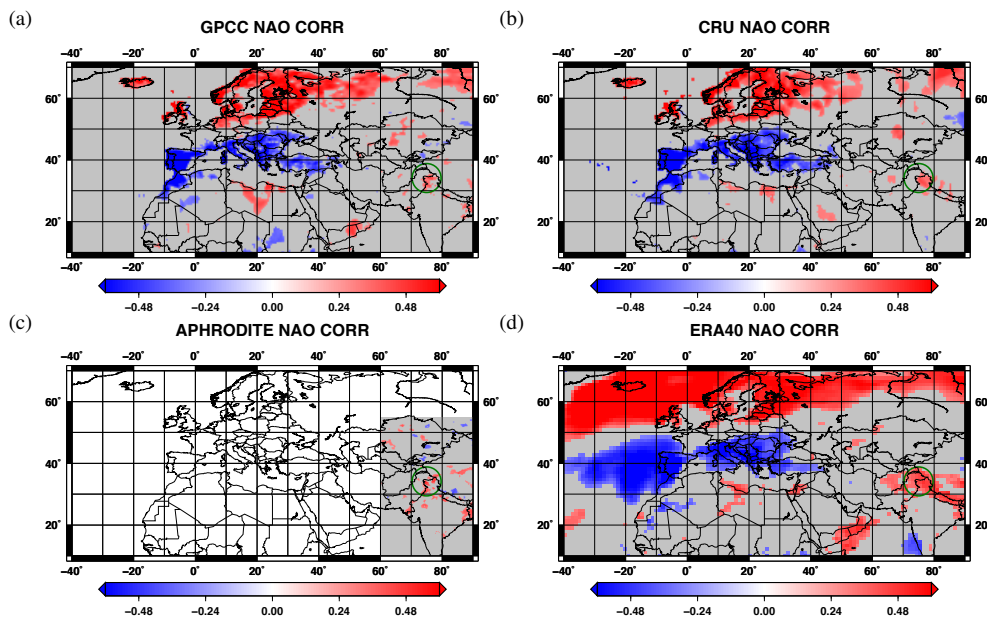


Fig. 2.2: Correlation coefficients between NAO and winter precipitation from (a) GPCC, (b) CRU, (c) APHRODITE and (d) ERA40. Colours indicate statistically-significant correlations at the 95% confidence level. Non-significant correlations are marked in grey. The green circle highlights the area of positive correlation centred on HKK.

To identify the major sources of the humidity transported to the HKK region, we have used the ERA40 data to estimate the mean moisture transport in DJFM, integrated vertically from 250 to 1000 hPa in the atmospheric column. Fig. 2.3a shows the transport vectors superimposed on the spatial map of the significant correlations between the NAO and the intensity of moisture transport (that is, the modulus of the transport vector). The figure shows that moisture, originating mainly from the northern Arabian Sea and the Red Sea, is transported towards HKK through the Persian Gulf. A comparatively smaller moisture contribution comes from the Mediterranean area,

though, on average, moisture from that area deviates north-eastward and affects mainly the regions north of HKK. The relatively small transport of Atlantic humidity over the Sahara region deviates southward before reaching the Red Sea, contributing minimally to the moisture channel from the Arabian area to the HKK region. As expected, significant positive correlations between NAO and the intensity of moisture transport occur over central-western Europe, while negative correlations occur across all the Mediterranean area, as shown by Hurrell (1995). Statistically significant, positive correlations are found 1) over a thin zonal strip in eastern Africa, between about 15°N and 25°N and 2) starting from the meridional Arabian peninsula and extending eastward to the southern Persian Gulf, part of the northern Arabian Sea, south western Iran, western Afghanistan and Pakistan, reaching western India and, to the north, the HKK. The two regions of positive correlation mentioned above are contiguous to each other, suggesting inter-dependence between the two signals. However, it is important to stress that, on average, humidity from region 1) does not flow directly into region 2), but it rather deviates southward, as shown by the vectors of moisture transport superimposed on the correlation map.

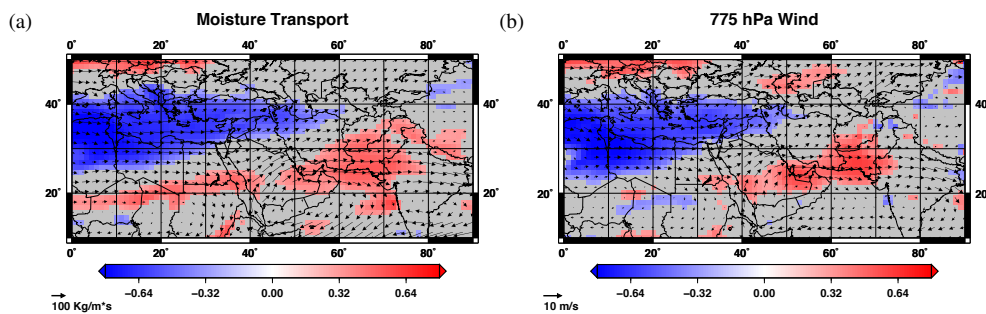


Fig. 2.3: (a) Mean moisture transport during Winter (vectors) and correlation coefficients between NAOI and the intensity of moisture transport (colour map). Colours are used for statistically significant correlations at the 95% confidence level, grey indicates non-significant correlations. (b) The same for wind at 775 hPa.

Positive and negative NAO composites of moisture transport are shown in Figs. 2.4a and 2.4b, respectively. The main differences between the two pictures occur in the Mediterranean region, where the overall transport is weaker during the positive NAO phase. In this region, however, moisture transport has an important southward component during the positive NAO phase. As a result, a fraction of the Mediterranean humidity reaches the Arabian area and flows into the main moisture channel from there to the HKK. Differences in the direction of moisture transport during the different NAO phases occur over the Arabian Peninsula, with a stronger northward (eastward) transport during the negative (positive) NAO phase. The intensity of moisture transport from the Arabian area to Pakistan is significantly larger during the positive NAO phase, consistently with the correlation analysis discussed above. The difference between positive and negative NAO composites of precipitable water obtained from ERA40, shown in Fig. 2.5a, is consistent with the considerations drawn for moisture transport. The Mediterranean region is characterized by a negative anomaly (that is, smaller values during the positive NAO phase), which is mainly caused by the weaker advection of moisture from the Atlantic (Hurrell, 1995). Positive anomalies are instead found over the southern and south-western side of the greater Himalayan chain, a region located south of the area where significant NAO-precipitation correlations are found in ERA40. This supports the view that moisture transport during the positive NAO phase sustains

wetter than normal conditions in this region, with a tendency of moisture to accumulate and to generate larger precipitation amounts over the slopes of the Himalayan range.

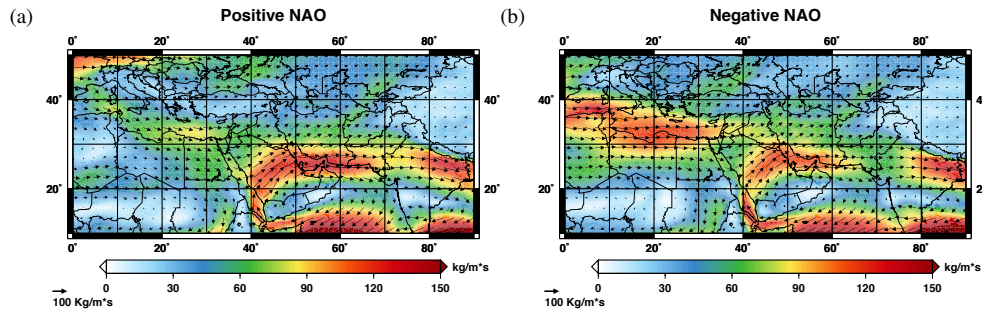


Fig. 2.4: Composites of moisture transport (vectors) and intensity of moisture transport (color map) for (a) positive NAO and (b) negative NAO winters.

Since water vapour essentially resides in the lower troposphere below 500 hPa, the lower-level atmospheric circulation is expected to contribute significantly to the vertically integrated total moisture transport. Similarly to Fig. 2.3a, Fig. 2.3b shows the mean DJFM wind fields computed at 775 hPa for the ERA40 reanalysis, superimposed on the spatial map of the significant correlations between the NAO and the intensity of 775 hPa winds. The wind patterns depicted in the figure confirm the previous considerations and highlight the role that the lower tropospheric circulation plays for the transport of moisture toward the HKK. The map of the correlation coefficients displayed in Fig. 2.3b, compared to that of moisture transport, shows that the NAO-induced anomalies in the intensity of moisture transport are associated with similar wind anomalies over Europe, the Mediterranean and over a region extending from the Arabian Peninsula to Pakistan. We do not find similar correlation patterns over North Africa: over this region, the NAO-moisture transport and NAO-wind correlation are more similar if we consider wind at 700 hPa and above (not shown here). The intensification of low tropospheric winds over the Arabian Peninsula, the northern Arabian Sea and Pakistan during the positive NAO phase could ensue from the vertical propagation of NAO-related changes occurring higher in the troposphere.

While the discussed changes in lower tropospheric circulation certainly play a major role in determining the enhanced moisture transport from the Arabian area to Pakistan during positive NAO events, wind is not the only variable influencing moisture transport. In Fig. 2.5b we show the difference between the positive and the negative NAO composites of evaporation: during the positive NAO phase, enhanced evaporation occurs from the Red Sea, the Persian Gulf, the northern Arabian Sea and the south-eastern Mediterranean. As discussed above, moisture from these sources converges over the Arabian Peninsula and is transported towards Pakistan, giving a major contribution to atmospheric moisture in the HKK. The evaporation signal from the Red Sea, the Persian Gulf and the northern Arabian Sea is associated with coherent signals in surface wind speed and sea surface temperature, as shown in Fig. 2.5c and Fig. 2.5d, respectively. During the positive NAO phase, ERA40 shows high surface wind speed over the Red Sea (note the very good correspondence with the evaporation anomalies), the Persian Gulf (significant correlations in the southern part, where the evaporation anomaly is stronger than elsewhere), and the northern Arabian Sea (significant correlations in the northernmost part of the region and south of about 20-15°), as well as high sea surface temperatures in a portion of the northern Arabian Sea, roughly corresponding to the area where the wind speed signal is not significant. Although it could be difficult to

associate the surface wind anomalies with the changes in the upper level circulation, owing to the strong influence of surface conditions, a link between the two seems reasonable. The whole picture obtained by from Figs. 2.5c and 2.5d reproduces well the signal of evaporation from the reservoirs observed in Fig. 2.5b.

Our results suggest that the dominant path through which the NAO could induce higher evaporation is the intensification of surface winds. During the positive NAO phase, the evaporation anomaly in the south eastern Mediterranean is associated with dry air conditions (Fig. 2.5a) and a negative anomaly in the intensity of moisture transport (see Figs. 2.3a and 2.4). However, winds mostly point to the South-East (as indicated by the moisture transport shown in Fig. 2.4a), transporting the available humidity toward the Arabian area and, from there, towards the HKK. This could lead to a higher contribution of the Mediterranean to the humidity transported toward the HKK during the positive NAO phase. In the north western Mediterranean, lower evaporation occurs during the positive NAO phase, coherently with the higher sea level pressure and the associated weaker surface winds which overcome the effect of the drier air. As shown in Fig. 2.5b, negative evaporation anomalies occur also in the Caspian Sea (with concordant signals in surface wind speed and sea surface temperature) and the north eastern Black Sea. Finally, significant evaporation anomalies are observed over land, mainly in Europe and North Africa, but with lower absolute values owing to the lower evaporation rates occurring in these regions.

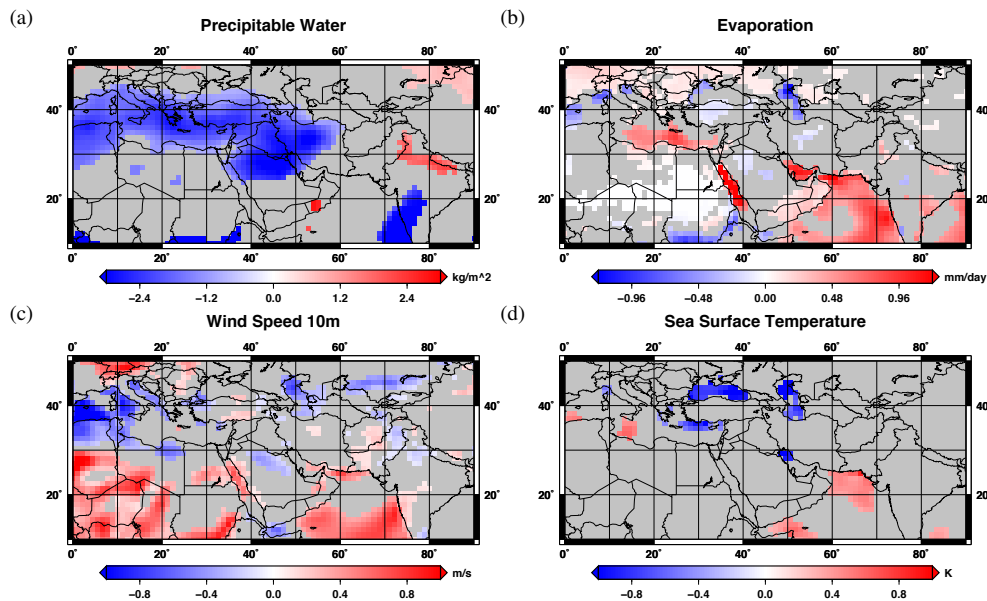


Fig. 2.5: Difference between the positive and the negative NAO composites of (a) precipitable water, (b) evaporation, (c) 10 m wind speed and (d) sea surface temperature. Colours indicate statistically significant values at the 95% confidence level; grey indicates non-significant values.

To summarize, winter precipitation in the Hindu-Kush Karakoram (HKK), an essential water input for the area is associated with the arrival of westerly perturbations originating from the Mediterranean and north eastern Atlantic regions. We have investigated how the North Atlantic Oscillation (NAO) affects winter precipitation in the HKK, focusing on the NAO-related effects on moisture transport. The existence of correlations between NAO and winter precipitation in the HKK is well known, what is new in our study is that we have identified the transport mechanisms which are at the origin of this correlation. We have shown, in particular, that the humidity transported to the HKK region mostly comes from the Arabian area, where moisture transports from the northern Arabian Sea, the Persian Gulf, the Red Sea and, to a lesser extent, from the

Mediterranean converge. Moisture transport is enhanced during the positive NAO phase and, as a consequence, wetter conditions are found over northern Pakistan and northern India than during negative NAO winters. We have suggested a mechanism by which the intensified moisture transport during the positive NAO phase occurs as an effect of changes in tropospheric circulation and in the evaporation from the reservoirs mentioned above.

During the positive NAO phase, an intensification of lower tropospheric westerly winds from the Arabian area towards Pakistan occurs, possibly as a result of the vertical propagation of the NAO-induced intensification of the subtropical Asian jet in the upper troposphere. Simultaneously, enhanced evaporation occurs from the Red Sea, the Persian Gulf and the northern Arabian Sea, associated with positive anomalies of surface wind speed and sea surface temperatures. A stronger southward component of the winds over the Mediterranean during the positive NAO phase represents a further contribution to the moisture reaching the Arabian area. Here, the increased humidity and the intensification of winds combine to give enhanced moisture transport towards the HKK. The extra moisture that accumulates over northern Pakistan and northern India during the positive NAO phase is picked up by the WWP, so that greater precipitation amounts are released as the WWP reaches the steep mountain slopes of the HKK.

References

ARCHER, D. R. AND H. J. FOWLER (2004): Spatial and temporal variations in precipitation in the Upper Indus Basin, global teleconnections and hydrological implications. *Hydrology and Earth System Sciences*, 8 (1), 47–61.

ARORA VK, SCINOCCA JF, BOER GJ, CHRISTIAN JR, DENMAN KL, FLATO GM, KHARIN VV, LEE WG, MERRYFIELD WJ (2011): Carbon emission limits required to satisfy future representative concentration pathways of greenhouse gases. *Geophys Res Lett* 38, L05805, DOI 10.1029/2010GL046270.

BELLOUIN N., RAE J., JONES A., JOHNSON C., HAYWOOD J., BOUCHER O. (2011): Aerosol forcing in the Climate Model Intercomparison Project (CMIP5) simulations by HadGEM2-ES and the role of ammonium nitrate. *J Geophys Res* 116, D20206, DOI 10.1029/2011JD016074.

BENTSEN M, BETHKE I, DEBERNARD JB, IVERSEN T, KIRKEVAG A, SELAND Ø, DRANGE H, ROELANDT C, SEIERSTAD IA, HOOSE C, KRISTJANSSON JE (2013): The Norwegian Earth System Model, NorESM1-M - Part 1: Description and basic evaluation of the physical climate. *Geo sci Model Dev* 6:687–720, DOI 10.5194/gmd-6-687-2013.

BI D., DIX M., MARSLAND S., O'FARRELL S., RASHID H., UOTILA P., HIRST A., KOWALCZYK E., GOLEBIEWSKI M., SULLIVAN A., YAN H., HANNAH N., FRANKLIN C., SUN Z., VOHRALIK P., WATTERSON I., ZHOU X., FIEDLER R., COLLIER M., MA Y., NOONAN J., STEVENS L., UHE P., ZHU H., GRIFFIES S., HILL R., HARRIS C., PURI K. (2013): The ACCESS coupled model: description, control climate and evaluation. *Aust Met Oceanogr J* 63, 41–64.

DAVINI P., CAGNAZZO C., FOGLI PG., MANZINI E., GUALDI S., NAVARRA A. (2013): European blocking and Atlantic jet stream variability in the NCEP/NCAR reanalysis and the CMCC-CMS climate model. *Clim Dyn* DOI 10.1007/s00382-013-1873-y

DELWORTH TL, et AL. (2006): GFDL's CM2 GlobalCoupled Climate Models. Part I: Formulation and Simulation Characteristics. *J Climate* 19:643–674, DOI 10.1175/JCLI3629.1.

GIORGETTA MA, et AL (2013): Climate and carbon cycle changes from 1850 to 2100 in MPI-ESM simulations for the Coupled Model Intercomparison Project phase 5. *Journal of Advances in Modeling Earth Systems* 5:572–597, DOI 10.1002/jame.20038.

HAZELEGER W., WANG X., SEVERIJNS C., STEFANESCU S., BINTANJA R., STERL A., WYSER K., SEMMLER T., YANG S., VAN DEN HURK B., VAN NOIJE T., VAN DER LINDEN E., VAN DER WIEL K. (2012): EC-earth v2.2: description and validation of a new seamless earth system prediction model. *Clim Dyn* 39:2611–2629, DOI 10.1007/s00382-011-1228-5.

HOURDIN F., FOIJOLS MA., CODRON F., GUEMAS V., DUFRESNE JL., BONY S., DENVIL S., GUEZ L., LOTT F., GHATTAS J., BRACONNOT P., MARTI O., MEURDESIOIF Y., BOPP L. (2013): Impact of the LMDZ atmospheric grid configuration on the climate and sensitivity of the IPSL-CM5A coupled model. *Clim Dyn* 40:2167–2192, DOI 10.1007/s00382-012-1411-3.

HURRELL, J. W., Y. KUSHNIR, G. OTTERSEN, and M. VISBECK (2003): An overview of the North Atlantic Oscillation. *The North Atlantic Oscillation: Climatic Significance and Environmental Impact*, J. W. H. et AL., Ed., American Geophysical Union, Vol. 134, 1–35.

HURRELL J.W., HOLLAND M.M., GENT P.R., GHAN S., KAY J.E., KUSHNER P.J., LAMARQUE J.F., LARGE W.G., LAWRENCE D., LINDSAY K., LIPSCOMB W.H., LONG M.C., MAHOWALD N., MARSH D.R., NEALE R.B., RASCH P., VAVRUS S., VERTENSTEIN M., BADER D., COLLINS W.D., HACK J.J., KIEHL J., MARSHALL S. (2013): The Community Earth System Model: A Framework for Collaborative research. *Bull Amer Meteor Soc* 94:1339–1360, DOI 10.1175/BAMS-D-12-00121.1.

KAUFMAN Y.J., FRASER R.S. (1997): The effect of smoke particles on clouds and climate forcing. *Science* 277:1636–1639, DOI 10.1126/science.277.5332.1636.

LAU K., KIM M., KIM K. (2006): Asian monsoon anomalies induced by aerosol direct forcing. *Clim Dynam* 26:855–864, DOI 10.1007/s00382-006-0114-z.

LEE J.Y., WANG B., KANG I.S., SHUKLA J., KUMAR A., KUG J.S., SCHEMM JKE, LUO JJ, YAMAGATA T., FU X., ALVES O., STERN B., ROSATI T., PARK CK (2010): How are seasonal prediction skills related to models' performance on mean state and annual cycle? *Clim Dyn* 35:267–183, DOI 10.1007/s00382-010-0857-4.

LIL, et AL (2013): The Flexible Global Ocean-Atmosphere-Land System Model: Grid-point Version 2: FGOALS-g2. *Adv Atmos Sci* 30:543–560, DOI 10.1007/s00376-012-2140-6.

MARTIN GM, et AL (2011): The HadGEM2 family of Met Office Unified Model climate configurations. *Geosci Model Dev* 4:723–757, DOI 10.5194/gmd-4-723-2011.

MEEHL GA., WASHINGTON WM., ARBLASTER JM., HU A., TENG H., TEBALDI C., STRAND WG., III JBW (2012): Climate System Response to External Forcings and Climate Change Projections in CCSM4. *J Climate* 25:3661–3683, DOI 10.1175/JCLI-D-11-00240.1.

PALAZZI, E., J. VON HARDENBERG, and A. PROVENZALE (2013): Precipitation in the Hindu-Kush Karakoram Himalaya: Observations and future scenarios. *J. Geophys. Res.*, 118, 85–100, doi:10.1029/2012JD018697.

RAMANATHAN V., CHUNG C., KIM D., BETTGE T., BUJA L., KIEHL JT., WASHINGTON WM., FU Q., SIKKA DR., WILD M. (2005): Atmospheric brown clouds: Impacts on south asian climate and hydrological cycle. *Proc Natl Acad Sci* 102:5326–5333, DOI 10.1073/pnas.0500656102.

RASMUSSEN R., BAKER B., KOCHENDORFER J., MEYERS T., LANDOLT S., FISCHER AP., BLACK J., THERIAULT JM., KUCERA .P, GOCHIS D., SMITH C., NITU R., HALL M., IKEDA K., GUTMANN E. (2012): How well are we measuring snow: the NOAA/FAA/NCAR winter precipitation test bed. *Bull Amer Meteor Soc* 93:811–829, DOI 10.1175/BAMS-D-11-00052.1.

ROTSTAYN LD., JEFFREY S.J, COLLIER MA., DRAVITZKI SM., HIRST AC., SYKTUS JI., WONG KK. (2012): Aerosol- and greenhouse gas-induced changes in summer rainfall and circulation in the Australasian region: a study using single-forcing climat esimulations. *Atmos Chem Phys* 12:6377–6404, DOI 10.5194/acp-12-6377-2012.

SCOCIMARRO E., GUALDI S., BELLUCCI A., SANNA A., FOGLI PG., MANZINI E., VICHI M., ODDOP., NAVARRA A. (2011): Effects of Tropical Cyclones on Ocean Heat Transport in a High Resolution Coupled General Circulation Model. *J Climate* 24:4368–4384, DOI 10.1175/2011JCLI4104.1.

SOLOMON S., QIN D., MANNING M., CHEN Z., MARQUIS M., AVERYT K.B., TIGNOR M., MILLER H.L. (2007): Climate Change 2007 - The Physical Science Basis: Working Group I Contribution to the *Fourth Assessment Report of the IPCC*. Cambridge University Press.

SYED, F. S., F. GIORGI, J. S. PAL, and M. P. KING (2006): Effect of remote forcings on the winter precipitation of central southwest Asia part 1: observations. *Theor. Appl. Climatol.*, 86, 147160, doi:10.1007/s00704-005-0217-1.

SYED, F. S., F. GIORGI, J. S. PAL, AND K. KEAY (2010): Regional climate model simulation of winter climate over CentralSouthwest Asia, with emphasis on NAO and ENSO effects. *Int. J. Climatol.*, 30, 220235, doi:10.1002/joc.1887.

SONG Z, QIAO F, SONG Y (2012): Response of the equatorial basin-wide SST to wave mixing in a climate model: An amendment to tropical bias. *J Geophys Res* 117, C00J26, DOI 10.1029/2012JC007931.

TAYLOR KE., STOUFFER RJ., MEEHL GA. (2012): An overview of cmip5 and the experiment design. *Bull Amer Meteor Soc* 93:485–498, DOI <http://dx.doi.org/10.1175/BAMS-D-11-00094.1>.

TRENBERTH KE., DAI A., RASMUSSEN RM., PARSONS DB. (2003): The changing character of precipitation. *Bull Amer Meteor Soc* 84:1205–1217, DOI <http://dx.doi.org/10.1175/BAMS-84-9-1205>.

VOLDOIRE A., et AL (2013): The CNRM-CM5.1 global climate model: description and basic evaluation. *Clim Dyn* 40:2091–2121, DOI 10.1007/s00382-011-1259-y.

VOLODIN EM., DIANSKII NA., GUSEV AV. (2010): Simulating present-day climate with the INMCM4.0 coupled model of the atmospheric and oceanic general circulations. *Izvestiya, Atmos Ocean Phys* 46:414–431, DOI 10.1134/S000143381004002X.

WATANABE S., HAJIMA T., SUDO K., NAGASHIMA T., TAKEMURA T., OKAJIMA H., NOZAWA .T, KAWASE H., ABE M., YOKOHATA T., ISE T., SATO H., KATO E., TAKATA K., EMORI S., KAWAMIYA M. (2011): MIROC-ESM 2010: model description and basic results of CMIP5-20c3m experiments. *Geosci Model Dev* 4:845–872, DOI 10.5194/gmd-4-845-2011.

WILCOX L.J., HIGHWOOD E.J., DUNSTONE N.J. (2013): The influence of anthropogenic aerosol on multi-decadal variations of historical global climate. *Environ Res Lett* 8, DOI 10.1088/1748-9326/8/2/024033.

WU T., LI W., JI J., XIN X., LI L., WANG Z., ZHANG Y., LI J., ZHANG F., WEI M., SHI X., WU F., ZHANG L., CHU M., JIE W., LIU Y., WANG F., LIU X., LI Q., DONG M., LIANG X., GAO Y., ZHANG J. (2013): Global carbon budgets simulated by the Beijing Climate Center Climate System Model for the last century. *J Geophys Res Atmos* 118:4326–4347, DOI 10.1002/jgrd.50320.

YADAV, R. K., K. R. KUMAR, and M. RAJEEVAN (2009): Increasing influence of ENSO and decreasing influence of AO/NAO in the recent decades over northwest India winter precipitation. *J. Geophys. Res.*, 114, doi:doi:10.1029/2008JD011318.

YADAV, R. K., K. R. KUMAR, and M. RAJEEVAN (2012): Characteristic features of winter precipitation and its variability over northwest India. *J. Earth Syst. Sci.*, 121, 611–623.

YUKIMOTO S., ADACHI Y., HOSAKA M., SAKAMI T., YOSHIMURA H., HIRABARA M., TANAKA TY., SHINDO E., TSUJINO H., DEUSHI M., MIZUTA R., YABU S., OBATA A., NAKANO H., KOSHIRO T., OSE T., KITO A. (2012): A New Global Climate Model of the Meteorological Research Institute: MRI-CGCM3 – Model Description and Basic Performance. *J Meteor Soc Japan Ser II* 90A:23–64, DOI 10.2151/jmsj.2012-A02.

D2.6.c: “Estimation of the changes in the hydrological cycle, snow cover and water availability in high altitude areas”

Author: S. Terzago
CNR-ISAC, Torino

Contributors:

E. Palazzi, J. von Hardenberg, A. Provenzale
CNR-ISAC, Torino

C. Cassardo
University of Torino, Dept. of Physics

U. Morra di Cella, E. Cremonese
ARPA VdA

This pilot study has the objective of estimating recent and future changes in the hydrological cycle, snow cover and water availability in high altitude areas.

In the first part we focus on the Hindu-Kush-Karakoram-Himalaya (HKKH) mountain range, where glaciers and snowpack are key features of the environment and provide water to about 1.5 billion people living in surrounding areas. Despite their importance, the climatic features concerning the snowpack spatial and temporal variability are still poorly known, owing to the insufficient availability of surface observations. We investigate how the snowpack is represented in the Reanalyses (ERA-INTERIM/Land and 20th Century Reanalysis), by the Global Climate Models included in the Coupled Model Intercomparison Project Phase 5 (CMIP5) and by the EC-Earth global climate model, which is run at CNR-ISAC. We compare all these product outputs over a common period and highlight common features and differences in order to evaluate the uncertainty on the estimate of the snow resources. We evaluate the GCMs snow depth projections for the 21st century and the expected changes of the snowpack in two climate change scenarios, RCP4.5 and RCP8.5.

In the second part we use two land surface models, UTOPIA and CHTESSEL, to simulate snow depth temporal variability and we compare them to assess their accuracy. We test the possibility to produce snow projections using physical/empirical snow models in off-line mode, forced by the atmospheric variables produced by the climate models. As in the previous case, we test the models performances over a control period, using the data collected in several sites in the Alps.

1. Introduction

This pilot study aims to provide information on the recent and expected changes in snow resources and in the hydrological cycle in high altitude areas, especially the Alps and the Hindu-Kush Karakorum Himalaya (HKKH) mountains. This result will be achieved by using state of art Global and Regional Climate Models (GCM, RCM), through the analysis and interpretation of the existing data and the new data obtained during the project.

As reported in the previous Deliverable D2.6.1c, the methodology adopted is based on a two-fold approach. The first approach is to directly use the snow projections provided by the climate models, possibly after application of a suitable downscaling procedure. The advantage is that the atmospheric and the surface-snow modules are interactive and therefore snow-change feedbacks on climate can be properly represented.

The second approach is to use physical/empirical models (i.e. CHTESSEL, UTOPIA, degree-day models) in off-line mode, forced by the atmospheric variables produced by climate models. In this case, the surface-atmosphere feedbacks cannot be represented but, on the other hand, it is possible to calibrate the snow models and, presumably, represent the snow dynamics more accurately for the region of interest.

We follow both approaches, with the aim to determine which is the most effective by comparing the results to the available past data.

2. Analysis of Global Climate Models snow depth historical and future simulations

The Hindu-Kush Karakoram Himalaya (HKKH) together with the Tibetan Plateau represents the largest mountain range in the world and the water melt from snowpack ensures a permanent water flow to the major Asian river systems such as Indus, Ganges, Brahmaputra, providing water for 1.5 billion people (Yao et al., 2012). The contribution of snow and glacier melt to the stream flow varies across the region and it is essential in areas that receive little summer precipitation such as the Hindu-Kush Karakoram and Western Himalaya (Liniger et al., 1998; Bookhagen et al., 2010). As a consequence, recent and future changes in snow abundance and distribution in HKKH mountains will impact on the water availability at lower elevations.

Despite the climatic issue may have a potentially big impact on the society, we do not know much about the current and past climate in the HKKH mountains, mainly because of the harsh environment and extreme weather conditions at high elevation. Surface observations are extremely rare and sparse both in space and time as they cover limited time periods. Meteorological satellites provide important information on the snow cover extension but an accurate estimation of the thickness is still an open issue. Currently available measurements are insufficient to draw a picture of snow depth characteristics and distribution in this area, thus we explored the simulations of the state-of-art Global Climate Models in the 5th Coupled Model Intercomparison Project (CMIP5, <http://cmip-pcmdi.llnl.gov/cmip5/>) experiment.

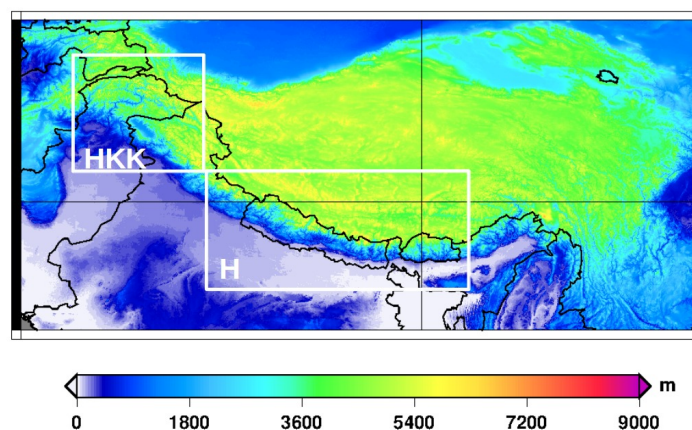


Fig. 1. Digital elevation model of the Hindu-Kush Karakoram Himalaya (HKKH) area. The two white boxes represent the Hindu-Kush Karakoram (HKK) and the Himalaya (H) subregions.

We investigated how current, state-of-the-art GCMs represent snow features in the HKKH in comparison to the ERA-Interim/Land reanalysis and the 20th Century Reanalysis products, in particular we analysed (i) the current characteristics of the snowpack in HKKH in terms of spatial distribution and seasonal cycle, comparing them to the reanalysis results; (ii) the changes detected in the historical period and expected by the end of the 21st century, in terms of snow abundance and snow cover extension.

The CMIP5 archive provides the output variables of the state-of-art Global Climate Models. Among all the models we selected those providing the snow depth variable. We included in the dataset also the EC-Earth model (Hazeleger et al., 2012) run at CNR-ISAC and whose snow depth variable is not stored in the CMIP5 archive. In total we considered 26 GCMs, reported in Table 1. Their spatial resolution ranges between 0.75-2.8° longitude, corresponding approx. to 75-300 km. For each model we used the simulations for the historical period (1850-2005) and the future projections under RCP4.5 and RCP8.5 scenarios (period 2006-2100).

Tab. 1. CMIP5 Global Climate Models providing the snow depth variable, and corresponding spatial resolution. The high spatial resolution models (highlighted in bold) have been retained for the analysis of the snow depth seasonal cycle and the future projections.

<i>Model</i>	<i>Institution</i>	<i>Spatial res.^o</i>
CMCC-CM	Euro-Mediterranean Centre for Climate Change	0.75
EC-Earth	EC-Earth Consortium	1.125
BCC-CSM1.1m	Beijing Climate Center, China	1.125
MRI-CGCM3	Meteorological Research Institute, Japan	1.125
CESM1-BGC	National Center for Atmospheric Research	1.25
CESM1-CAM5	National Center for Atmospheric Research	1.25
CESM1-FASTCHEM	National Center for Atmospheric Research	1.25
CNRM-CM5	Centre National de Recherches Météorologiques	1.4
MIROC5	University of Tokyo	1.4
ACCESS1-0	CSIRO/BOM, Australia	1.875
CMCC-CMS	Euro-Mediterranean Centre for Climate Change	1.875
CSIRO-Mk3-6-0	CSIRO, Australia	1.875
INM-CM4	Institute for Numerical Mathematics	2
CESM1-WACCM	National Center for Atmospheric Research	2.5
GISS-E2-H-CC	NASA Goddard Institute for Space Studies	2.5
GISS-E2-H	NASA Goddard Institute for Space Studies	2.5
GISS-E2-R-CC	NASA Goddard Institute for Space Studies	2.5
GISS-E2-R	NASA Goddard Institute for Space Studies	2.5
NorESM1-ME	Norwegian Climate Centre	2.5
NorESM1-M	Norwegian Climate Centre	2.5
BCC-csm1-1	Beijing Climate Center, China	2.8125
CanESM2	Canadian Centre for Climate Modelling and Analysis	2.8125
FGOALS-g2	LASG/CESS, China	2.8125
FIO-ESM	The First Institute of Oceanography, China	2.8125
MIROC-ESM-CHEM	Japan Agency for Marine-Earth Science and Technology	2.8125

The domain of study is the Hindu Kush Karakoram Himalaya (HKKH) mountain range, included between 68-105°E and 23-39° (Figure 1). This area has been subdivided into two climatically homogeneous subregions according to precipitation regimes: 1) the Hindu Kush-Karakoram (HKK) where rainfall is primarily due to Western Weather Patterns (WWP) and mainly occurs in the winter months, and 2) the Himalaya (H) where rainfall is related to the monsoons and therefore it mainly occurs in the warm season between June and September. This study aims to explore climate features in high-altitude areas thus we retained altitude higher than 1000 m a.s.l..

We examined how the different Global Climate Models represent the snow depth on a monthly and seasonal basis in HKKH. In this area the validation of the models with the “ground truth” is limited by the scarcity of observational snow depth data, thus, we used the ERA-Interim/Land and the 20th Century reanalyses as a reference. We found that in

HKKH models with high spatial resolution ($0.75\text{-}1.25^\circ$) are generally in better agreement with the reanalyses than those at lower spatial resolution. The high-resolution models show a winter snow depth peak in the Karakoram and decreasing values moving towards the Himalaya and the Tibetan plateau (Figure 2). In summer most of the models reports very shallow or negligible snow depth over the HKKH region. The Hindu-Kush Karakoram results snow covered while the Himalaya mountains are represented as mainly snow free, in agreement with MODIS satellite snow cover observations (Pu et al., 2007). Despite the Himalaya receives considerable amount of precipitation due to the monsoon, this precipitation does not contribute to create a durable snow depth because the high temperatures induce fast melting.

We explored how the high resolution GCMs simulates the snow seasonal cycle in the HKK and Himalaya domains. We selected the mountains above 1000 m a.s.l. and we calculated for each model the spatially averaged monthly snow depth in the period 1980-2005.

According to the high resolution GCMs the seasonal cycle of snow depth (i.e. the multiannual average of monthly thickness of the snowpack during the season from September to August) has a unimodal distribution with a maximum in February/March in both regions. The spread among the models is non-negligible, but they overall tend to overestimate snow depth compared to the ERA-Interim/Land reanalysis. In the HKK subregion the multi-model ensemble mean overestimates the snow depth values compared to ERA-Interim/Land and the 20th Century reanalyses, while in the Himalaya it lies inside the range of variability of the reanalyses. In the Himalaya, the difference between the reanalyses is larger, indicating higher uncertainty in the estimation of the snowpack thickness in this area.

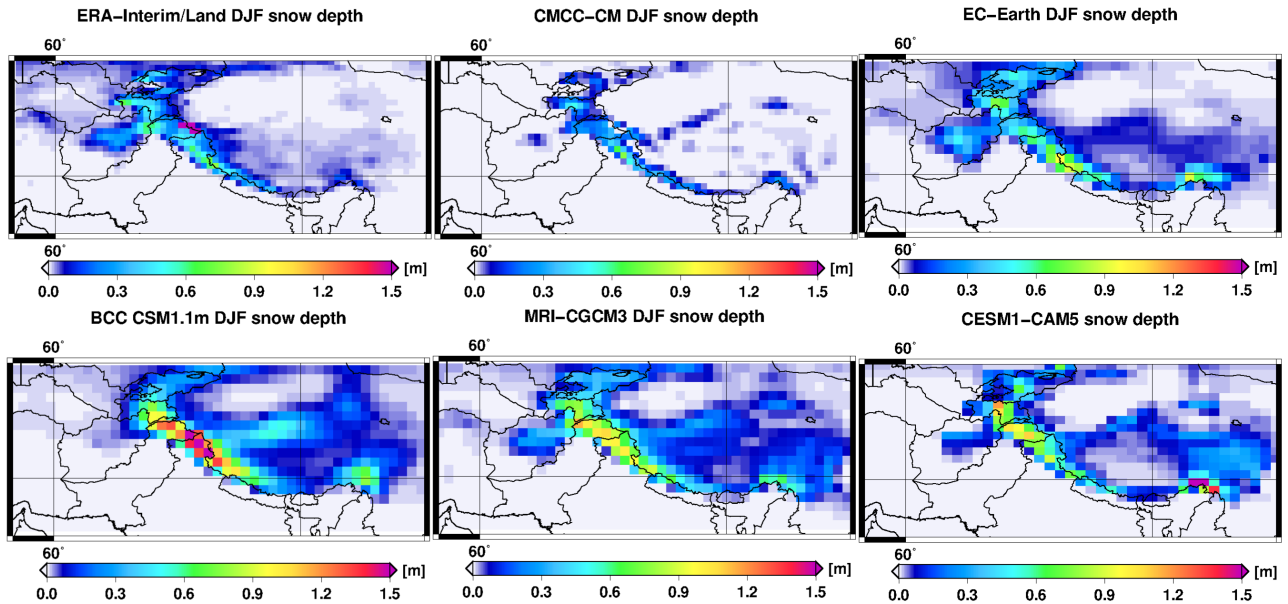


Fig. 2. Spatial distribution of the winter snow depth fields obtained from ERA-Interim/Land reanalysis and the high resolution ($0.75\text{-}1.25^\circ$ longitude) CMIP5 GCMs simulations. The maps represent winter multiannual averages over the period 1980-2005 and they are ordered according to decreasing spatial resolution.

We assessed the interannual variability of snow cover in the historical period and in the future projections under the RCP4.5 and RCP8.5 climate change scenarios (Figure 3). The climate projections for the future indicate a significant snow depth decrease between

17% and 39% in HKK and between 25% and 50% in the Himalaya depending on the scenario considered (RCP4.5 and RCP8.5 respectively). In the Himalayas the models project an earlier start of the snowpack melting that will anticipate from March to February, affecting the timing of the water discharge and the seasonal distribution of melting water in the valleys and low regions.

Despite the GCMs coarse resolution compared to the rapidly varying topography of mountain regions, the CMIP5 ensemble provides important information on the HKKH snow climatology and its expected changes in future decades. Absolute validation of GCM results against “ground truth” remains a challenge in such orographically complex areas, and this study highlights the need of a surface observations network as a priority for improving our current knowledge.

3. Assessment and validation of physical snow models

The second research approach aims to simulate snowpack temporal variability using physical or empirical models, in off-line mode, forced by atmospheric variables produced by large-scale climate models.

Climate models provide meteorological variables at coarse spatial and temporal resolution compared to weather station measurements. Thus we explore the reliability of the snow models simulations of the models depending on the "quality" and the spatio-temporal resolution of the initial data. In other words we carry out simulations with different types of input data, of gradually decreasing spatial resolution and/or "quality":

- (i) data of fully-equipped and innovative weather stations (the “ideal case”) measuring all the needed input variables with high level of accuracy;
- (ii) data of standard meteorological stations, which measure only the main variables. The other variables required by the snow models are derived by models themselves through their own parameterizations;
- (iii) large scale datasets with low temporal (3-6 hours) and spatial (~70 km) resolution and with a greater uncertainty in the measurements.

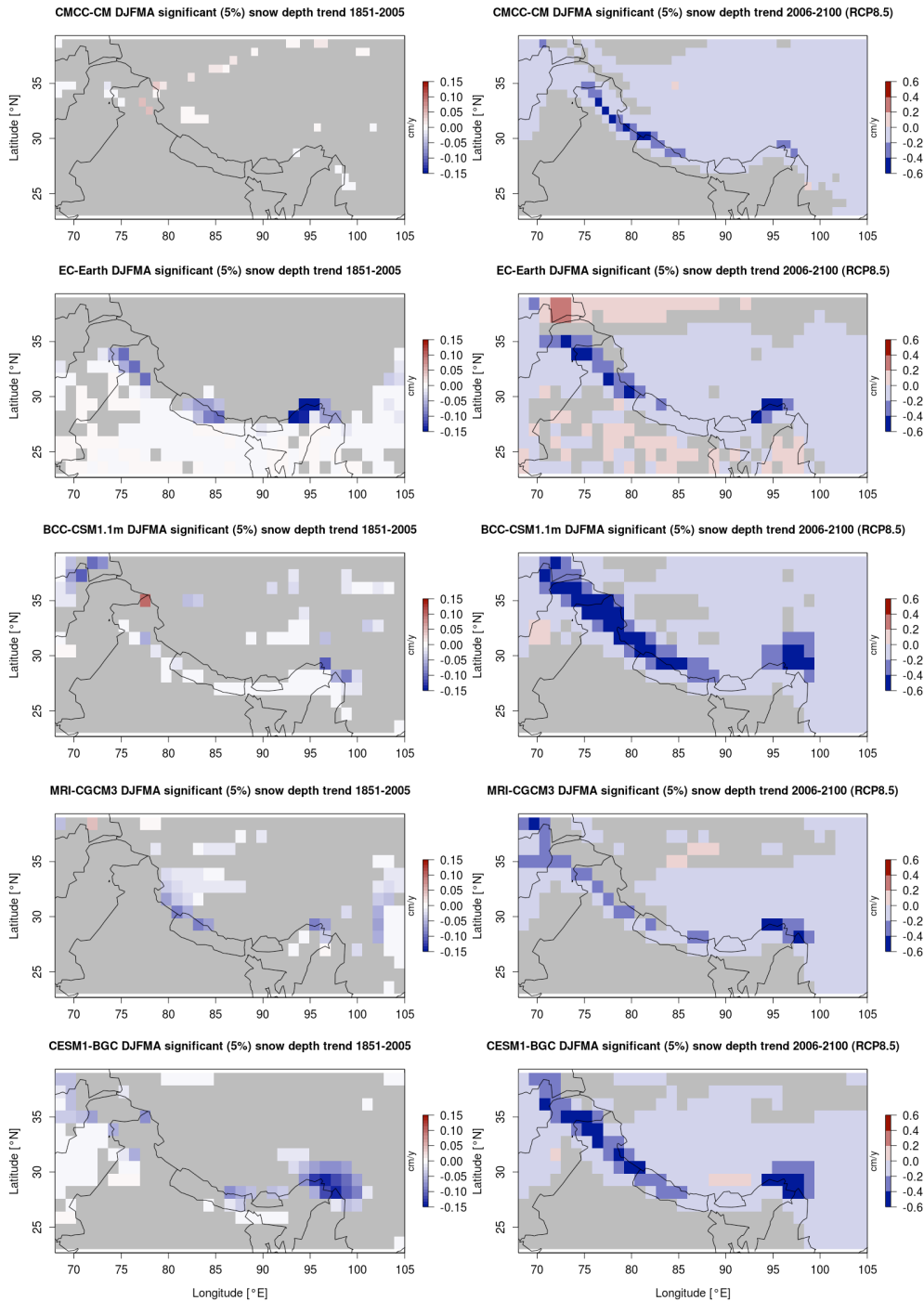


Fig. 3. GCMs DJFMA snow depth trends (significant at 95% confidence level) referring to the historical period 1851-2005 (left) and to the future projections (2006-2100) under the RCP8.5 scenario.

The goal is to identify the models that provide the best estimates even if they are forced to input data at low spatial resolution and greater uncertainty.

Through a collaboration with ARPA Valle d' Aosta we obtained the data of the nivometeorological observing site Torgnon, 2160 m a.s.l. (Aosta). This station is equipped with innovative instruments such as the OTT pluviometer (operating since mid 2012) and provides high accuracy measurements. Torgnon is thus an ideal site that provides high quality data.

We also considered nivo-meteorological measurements performed at the Colle Bercia station (2200 m a.s.l.), which is equipped with standard instrumentation and provides data since 2003. In this case, a preliminary analysis has been carried out to verify the quality of the measurements. In particular we checked precipitation data as rainfall and snowfall are particularly critical to measure at high altitude. For this station we identified the “snowfall events” as the days when precipitation $P > 0$ mm and temperature $T < 2^{\circ}\text{C}$. We compared the results to the snowfall events identified by the snow depth sensor and we found good agreement (Figure 4). This positive result support the use of this datasets as a forcing for the snow models, in fact the reliability of the initial data of precipitation is crucial to obtain a good estimate of the seasonal variability of the snow depth.

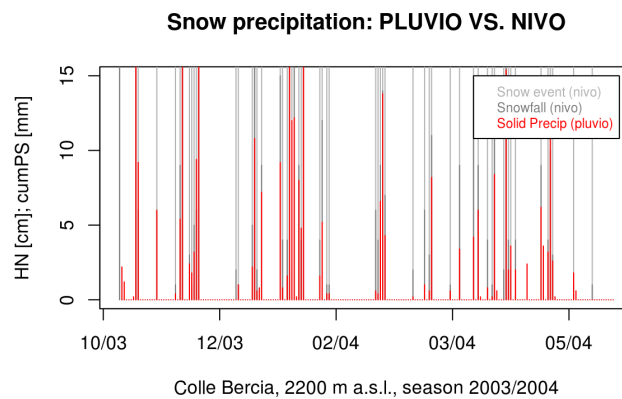


Fig. 4: Snowfall identified using snow-depth sensors data (light & dark grey) and snowfall derived using the combination of temperature (T) and precipitation (P) data, i.e. snowfall is defined as the precipitation amount when $P > 0$ mm & $T < 2^{\circ}\text{C}$ (red). Light grey lines are the snowfall events identified using snow gauges.

On the two sample stations mentioned above we tested and compared the two physical models: the University of Torino land-surface Process Interaction model in the Atmosphere (UTOPIA) and the Hydrology-Tiled ECMWF Scheme for Surface Exchange over Land (CHTESSEL).

Figure 4 (left) shows the simulations of the evolution of the snowpack in the site of Torgnon in the season 2012-2013 obtained using UTOPIA and CHTESSEL models, compared to the observations performed through a ultrasonic snow gauge. UTOPIA provides a good estimate of the characteristics of the snowpack, generally very close to the real conditions. CHTESSEL tends to underestimate the snow depth, mainly due to the excessive melting simulated at the beginning of the snow season.

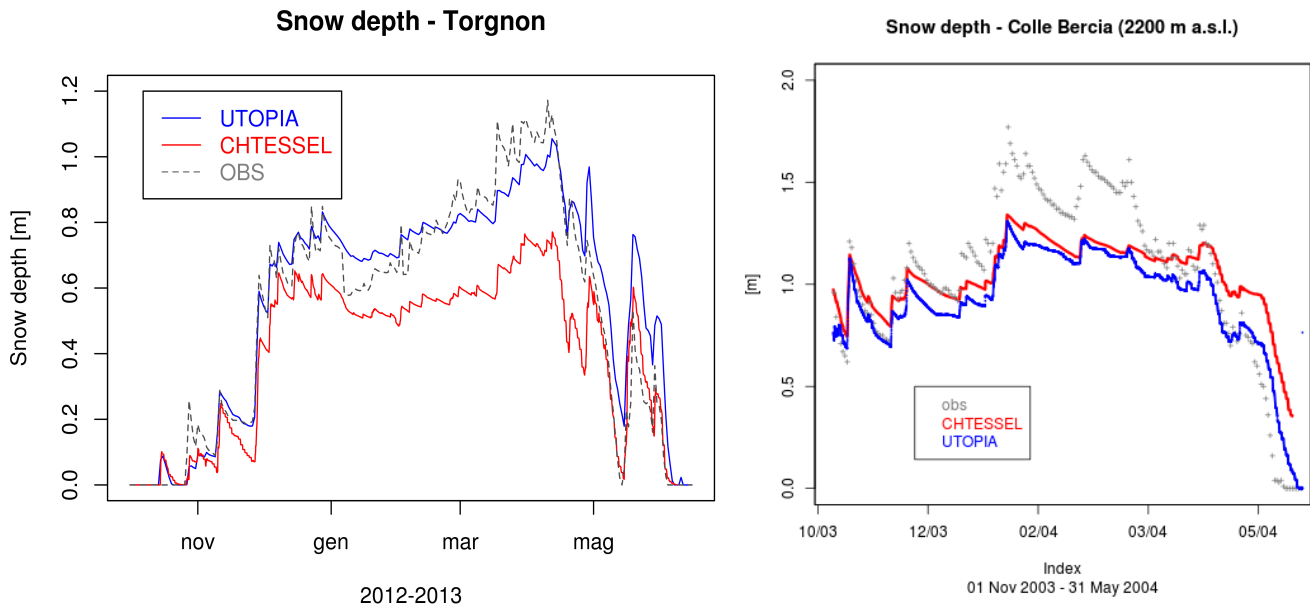


Fig. 4. Time evolution of the snowpack simulated with UTOPIA (blue), CHTESSEL (red) compared to the observations (grey) in the station of Torgnon (left) and Colle Bercia (right), in the Aosta Valley and Piedmont Alps respectively.

Figure 4 (right) shows the results for Colle Bercia station (2200 m a.s.l.). In this case the models adequately reproduce the processes of snowfall and melting of the mantle but they tend to underestimate the snowfall in case of intense events. The cause of this underestimation may be due to the fact that the models estimate the solid precipitation amount from the data recorded through a heated rain gauge. These tools are suitable for the measurement of the precipitation liquid but they tend to underestimate the solid precipitation. In fact their resistor is not able to melt quickly enough the snow that accumulates and obstructs the cup, thus producing a remarkable underestimation during intense events. Therefore, the discrepancy between the temporal evolution simulated by UTOPIA and CHTESSEL and the observations may be in part due to the quality of the forcing rather than to internal problems of the models. The total melting of the mantle simulated by UTOPIA occurs with a delay of approximately 7 days compared to the observations while CHTESSEL does not melt completely the snowpack.

These preliminary results suggest that the quality of the input data is crucial to obtain a good estimate of the seasonal snowpack, so it will be necessary to develop appropriate techniques for validating and correcting the stations measurements, in particular those of precipitation. This theme will be developed within the Special Project P2.

The following step will be to perform model simulations using low spatial and temporal resolution forcing, i.e. the ERAI-Interim reanalyses at about 70 km horizontal resolution and 6 hours temporal resolution, in order to evaluate the sensitivity of the models to the accuracy of the input data.

In the next months we will extend the snow model comparison including other physical and empirical models, i.e. Amundsen, S3M, Geotop and Achab-snow, working in collaboration with the Special Project P2.

Conclusions and Outlook

The analysis of the representation of the snowpack by state-of-art Global Climate Models in the HKKH region, compared to ERA-Interim/Land and 20th Century Reanalyses, allowed to assess the current uncertainty in the determination of the snow resources in orographically complex areas. A large-scale picture of the expected changes in the snow resources in the HKKH region has been obtained analysing the GCMs projections for the 21st century in the RCP4.5 and RCP8.5 scenarios. An important snow depth reduction is expected in the HKK and Himalaya regions in future decades. A detailed relation on the results of this study will be available in a paper currently under revision. Further work will focus on downscaling techniques, both dynamic and stochastic, to improve the spatial resolution of the currently available snow projections.

In the next months the physical and empirical snow models inter-comparison will be extended and we will identify the model/the set of models which can adequately reproduce the snowpack temporal evolution and which will be run to achieve high resolution snow projections.

D2.6.2e: “Multi-secular historical climate simulation for the Mediterranean area and comparison with paleoclimatic proxy data, to obtain a climatological history of Italy in the last one thousand years”

“Part 1: Simulations of the last 150 years climate with an Earth system models of intermediate complexity and preparation of paleoclimate simulations”

Author: E. Palazzi
CNR-ISAC, Torino

Contributors:

F. Toselli
University of Torino

J. von Hardenberg, A. Provenzale
CNR-ISAC, Torino

1. PlaSim

The Planet Simulator (PlaSim) is an Earth system Model of Intermediate Complexity (EMIC) that was developed at the Meteorological Institute of the University of Hamburg and can be used to run climate and paleo-climate simulations for time scales up to 10 thousand years, due to its medium complexity and associated less intensive computing requirements.

Compared to other state-of-the-art EMICs (Claussen, 2002), PlaSim has a more complex atmospheric model (the Portable University Model of the Atmosphere, PUMA) based on the moist primitive equations conserving momentum, mass, energy and moisture and including, as in the most comprehensive general circulation models (GCMs), all atmospheric processes, but with the limitation of less sophisticated parameterizations (Fraedrich et al., 2005).

The atmospheric model can be coupled to different ocean models besides using climatological sea surface temperatures (SSTs). These ocean models can be a mixed-layer ocean or the large-scale geostrophic ocean (LSG, Maier-Reimer et al., 1993). Besides the atmospheric and oceanic parts, a land surface model with biosphere and a module representing sea ice can also be included. A complete description of how the coupling between the various components is realized can be found in the PlaSim User Guide (http://www.mi.uni-hamburg.de/fileadmin/files/forschung/theomet/planet_simulator/downloads/PS_Users_Guide.pdf).

2. Model configurations, experiments, and methodology

Before running PlaSim over paleoclimatic time scales, we considered worthwhile testing the model ability in simulating the climate response to the CO₂ forcing over the last ~150 years and, in particular, in reproducing the observed global warming trend and changes

in total precipitation from 1850 to 2005, which is commonly referred to as the “historical period” in the simulations with climate models participating in state-of-the-art international intercomparison programs. Different PlaSim configurations as well as spatial resolution have been tested. We opted for only atmosphere-ocean coupling, testing both mixed-layer (ML) and LSG ocean models; we did not include the vegetation and sea ice models.

We run PlaSim at two horizontal resolutions, T21 and T42 corresponding to about 5.6° and 2.8° latitude-longitude respectively. We performed two different kinds of climate simulations:

1. Perpetual runs, aimed at generating average climate conditions for two years, 1850 and 2005, representative of a different CO₂ forcing, by running the model for 30 years (PUMA + ML at T21 and T42) and for 500 years (PUMA + LSG, at T21 only) by maintaining the appropriate CO₂ forcing for 1850 (285 ppmv CO₂) and for 2005 (379 ppmv CO₂). We called these runs “Perpetual 1850” and “Perpetual 2005” simulations.
2. Transient runs, aimed at generating a multi-year historical simulation, using both ocean model configurations and both atmospheric resolutions, from 1850 to 2005 (156 years), using the historical atmospheric concentrations of CO₂ available as global mean time series from the website at IIASA <http://tntcat.iiasa.ac.at/RcpDb/>.

The PlaSim outputs have been analysed in terms of

- Time series of global mean averages of surface temperature and total precipitation or averages over different latitudinal bands.
- Zonal means of surface temperature and total precipitation.
- Mean temperature and precipitation annual cycle.
- Spatial maps of the multiannual mean of annual or seasonal surface temperature and precipitation.

Since the climate of a PlaSim control run (50 years) was extensively analysed by the model developers and validated against ERA-40 reanalysis data (see http://www.mi.uni-hamburg.de/fileadmin/files/forschung/theomet/docs/pdf/PS_Climate_Report.pdf), we decided to focus the PlaSim evaluation by comparing the model outputs to the historical simulations from other state-of-the-art global models: 1) the EC-Earth GCM (Hazeleger et al., 2012) version 2.3, run at ISAC-CNR, and 2) an ensemble of Coupled Model Intercomparison Project Phase 5 (CMIP5) GCMs, available at the Program for Climate Model Diagnosis and Intercomparison (PCMDI) web page (<http://cmip-pcmdi.llnl.gov/cmip5/>). For specific cases, we have also used observation-based gridded datasets for comparison, for example the GPCP precipitation data.

In this report we indicate with “EC-Earth 1850” or “EC-Earth 2005” the average output of two twenty-years long simulations performed with the EC-Earth model for the periods 1850-1869 and 1986-2005, respectively, to be compared with the “Perpetual 1850” and “Perpetual 2005” PlaSim simulations. We use the term “GPCP 2005” to indicate, in the same way, the average output of GPCP in the period 1986-2005.

3. Global mean climatology from the analysis of the “perpetual runs”

Temperature and precipitation series

Figure 1 shows the temperature and precipitation series from the 30-years long “Perpetual 1850” and “Perpetual 2005” PlaSim simulations, performed coupling the

PUMA atmospheric model run at T42 and T21 horizontal resolutions with the Mixed-Layer Ocean. The figure shows that the model is able to respond to the 1850 and 2005 different CO₂ forcing, giving rise to different average temperature and precipitation values. At T21 (T42), a difference of about 1°C (slightly more than 1°C) between the 2005 and 1850 temperature values is detected. For the precipitation, the difference between the 2005 and 1850 values is around 0.1 mm/day at T42, while it is lower at T21. Moreover, it is clear from the figures that the horizontal resolution affects the absolute temperature and precipitation values, giving rise to higher values of both variables at T42 than at T21 spatial resolution.

Figure 2 shows the temperature and precipitation series obtained from the 500-years long perpetual runs using PUMA, run at T21 spatial resolution, coupled with LSG. We can see that, again, a difference of about 1°C (0.1 mm/day) can be found between the average 2005 and 1850 temperature (precipitation). It is also worth noting that the temperature and precipitation values found for this simulation are smaller compared to those found for the T21 and T42 runs performed with PUMA coupled to ML (more than 1°C difference for the temperature and more than 0.1 mm/day for precipitation).

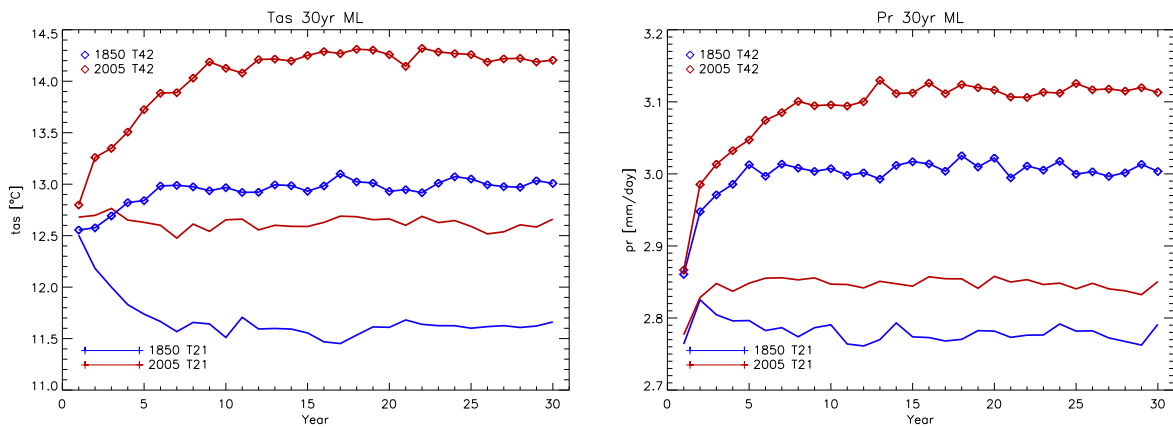


Fig. 1. Time series of temperature (left) and precipitation (right) for the 30-yr perpetual 1850 (blue lines) and 2005 (red lines) runs (T21 filled lines; T42 lines with symbols).

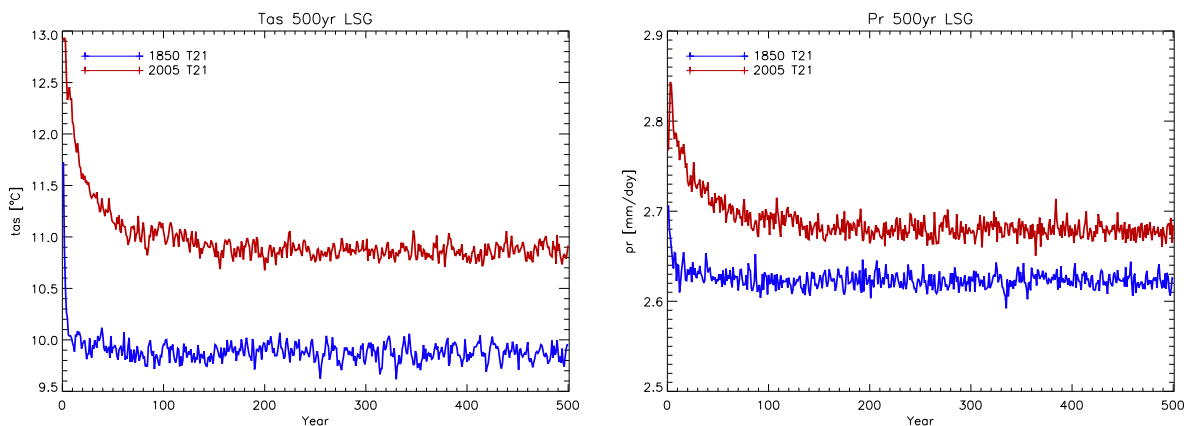


Fig. 2. Time series of temperature (left) and precipitation (right) for the 500-yr perpetual 1850 (blue lines) and 2005 (red lines) runs at T21 spatial resolution.

For the analysis of the 1850 and 2005 mean climatology, we averaged the precipitation and temperature values over the last 20 years of the perpetual 30yr-long simulation and

over the last 300 years of the 500yr-long simulation, thus excluding the period the model takes to reach its climate equilibrium.

Spatial maps of temperature and precipitation

Figure 3a shows the spatial maps of the multiannual mean annual mean temperature obtained from the perpetual 2005 PlaSim simulations (PUMA+ML at T21 and T42, PUMA+LSG at T21) and from the EC-Earth 2005 simulation.

In order to better highlight the differences between the three PlaSim simulations and EC-Earth we show in Fig. 3b the spatial map of the temperature difference between EC-Earth and the PlaSim outputs.

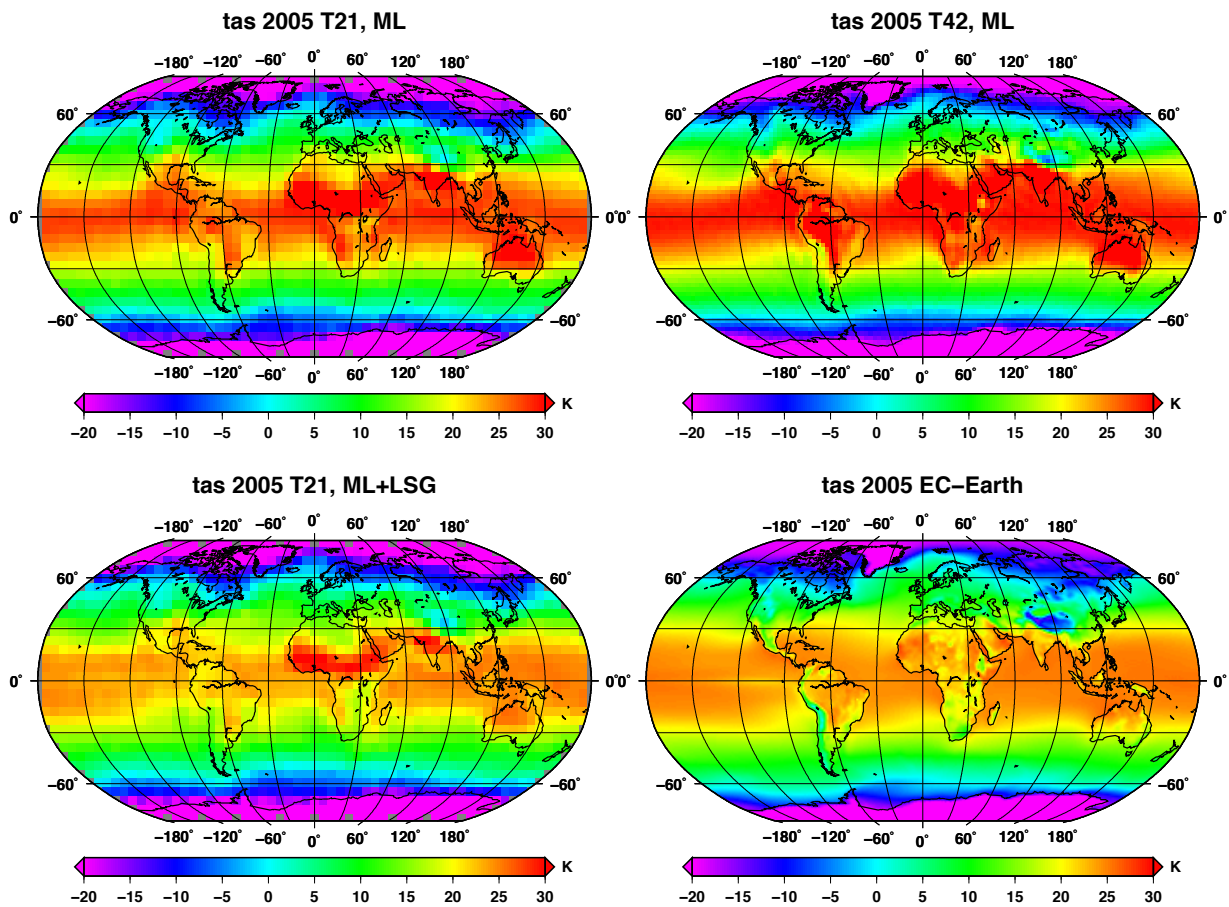


Fig. 3a. Spatial maps of 2005 surface temperature obtained from the “perennial 2005” PlaSim simulation at T21 (left column) and T42 (top right panel) spatial resolutions, with PUMA coupled to the ML ocean (top panels) or to LSG (bottom left). The spatial map of the EC-Earth 2005 temperature (multi-annual mean average over the years 1986-2005) is shown in the bottom right panel for comparison.

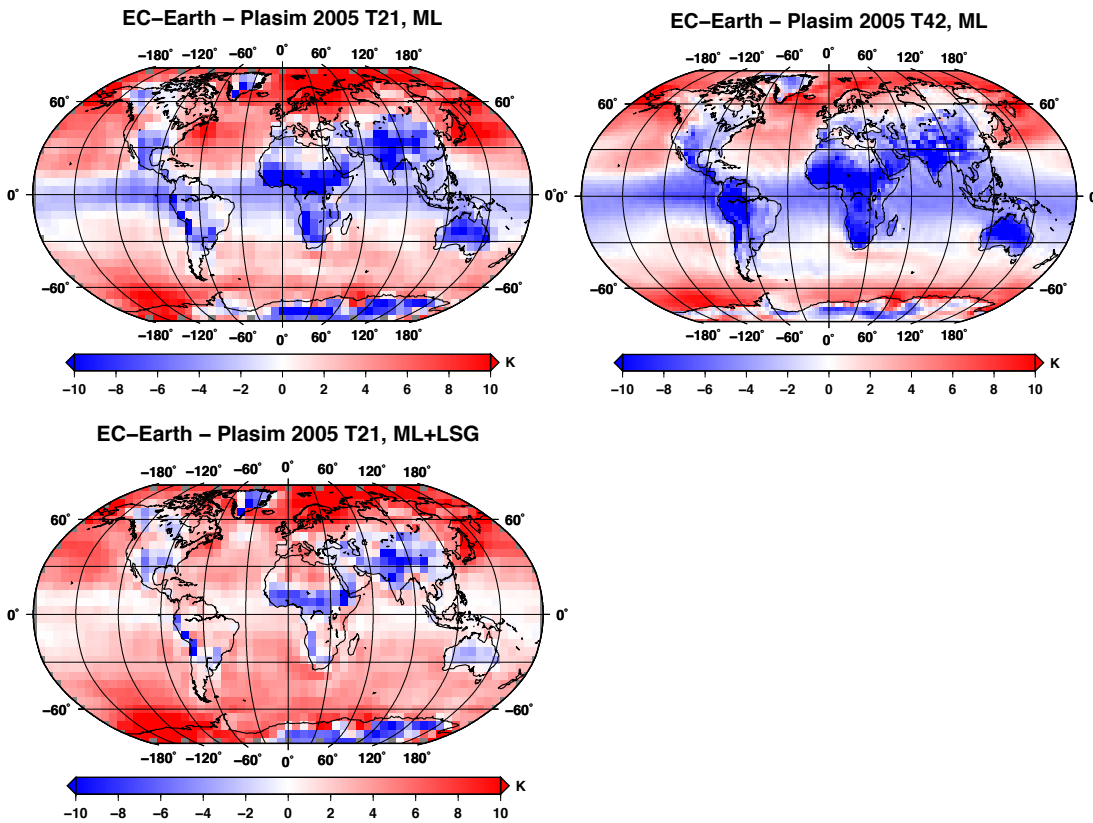


Fig. 3b. Spatial maps of 2005 surface temperature difference between EC-Earth and Plasim (perennial 2005 simulation at T21, T42 with PUMA coupled to the ML ocean and at T21 with PUMA coupled to LSG, from left to right).

PlaSIM-ML simulations exhibit a warm bias with respect to EC-Earth at both resolutions in the equatorial and tropical oceans, the Australian continent, overall in Africa, South-America, the Middle-East, the Indian sub-continent and the Tibetan Plateau. On the contrary, a cold bias of PlaSim-ML relative to the EC-Earth simulations is found in the mid-latitude and polar oceans. The PlaSim-LSG simulations exhibit a cold bias with respect to EC-Earth, except over the Indian sub-continent, the high-altitude regions of the Third Pole Environment, the Andes, and central Africa.

Figure 4 shows the same as Fig. 3a but for the precipitation; in this case, the GPCP 2005 precipitation map is also shown for comparison (bottom right panel).

The two PlaSim-ML simulations exhibit much higher precipitation amounts around the equator than EC-Earth and GPCP data, as well as with respect to the PlaSim-LSG simulation. All PlaSim simulations (particularly the PlaSim-ML simulations) do not display the double ITCZ structure found in EC-Earth and GPCP (and, in general, in the observations).

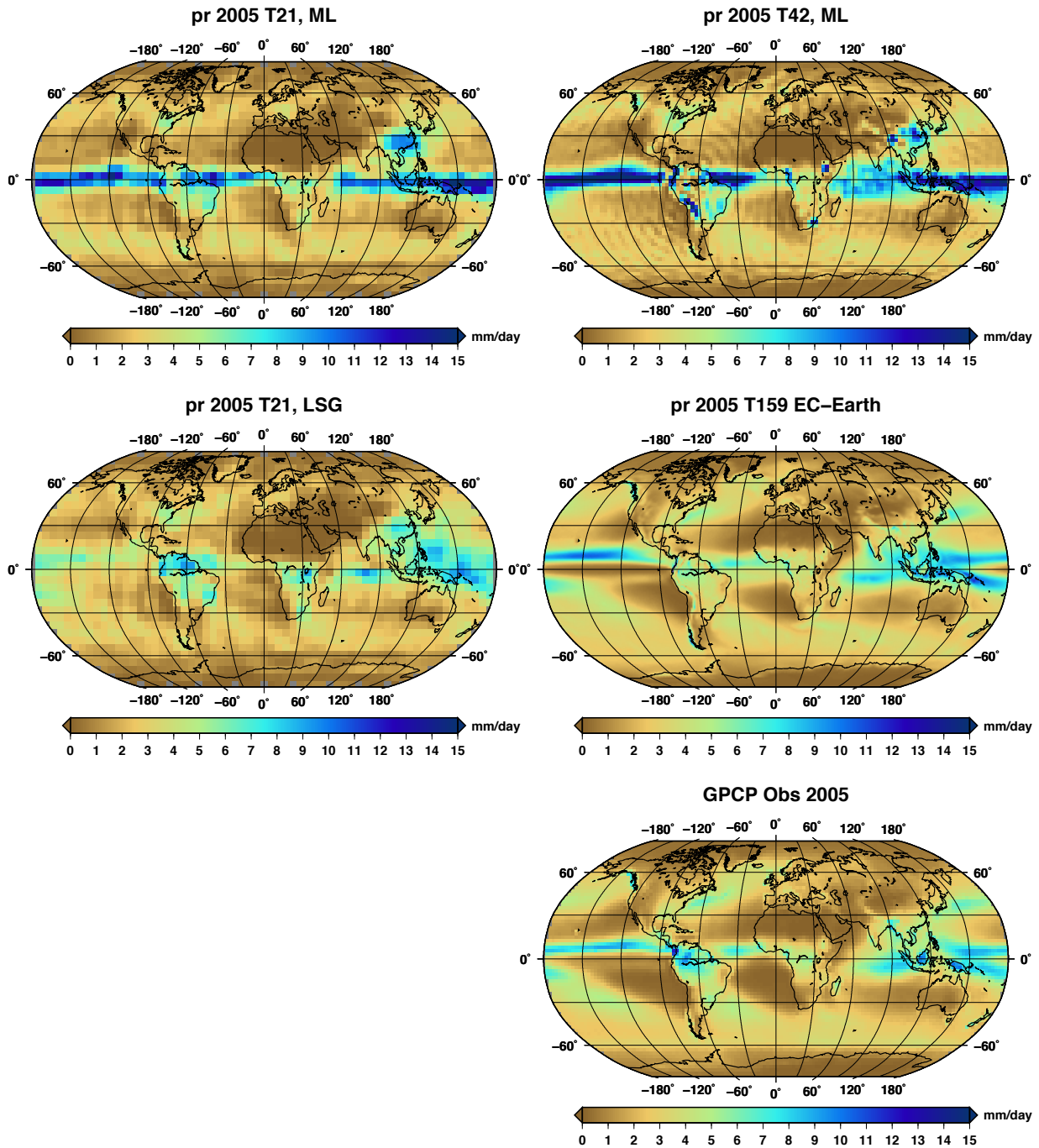


Fig. 4. The same as Figure 3, but for total precipitation. The GPCP 2005 observation-based precipitation (2.5° spatial resolution) is shown in the bottom right panel.

In order to better highlight the spatial distribution of the temperature and precipitation change between 2005 and 1850 conditions, we show in Figs. 5 and 6 the spatial maps of the difference between the 2005 and 1850 mean temperature and precipitation, respectively, from the three PlaSim simulations and from EC-Earth.

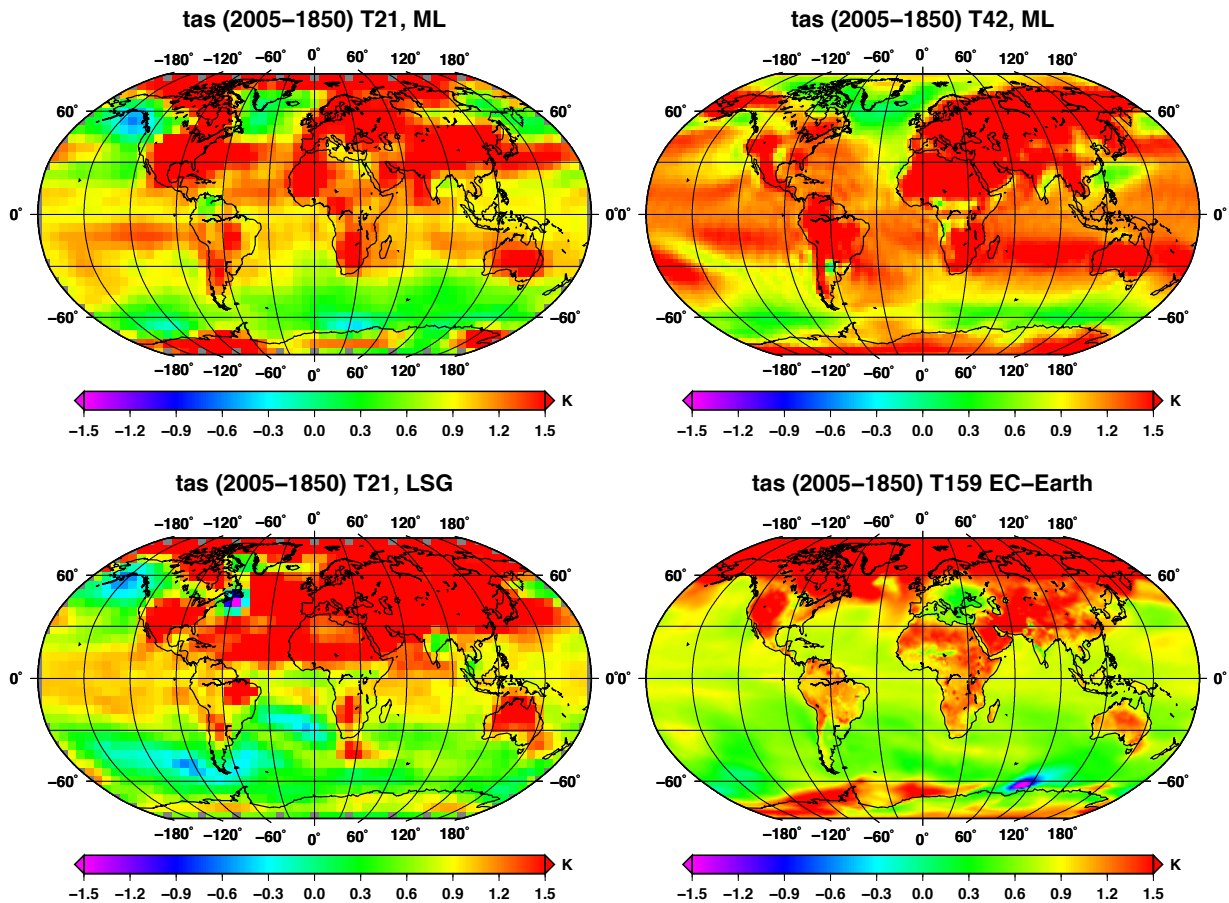


Fig. 5. Spatial maps of the surface temperature change in 2005 relative to 1850, obtained after subtracting the time-averaged value of the “perennial 1850” PlaSim simulation from the one of the “perennial 2005” simulation at T21 (left) and T42 (top right). The EC-Earth temperature change is also shown in the bottom right panel (2005 EC-Earth – 1850 EC-Earth).

Positive temperature differences between the 2005 and 1850 conditions are found in the three PlaSim simulations and in EC-Earth almost everywhere. However, with respect to EC-Earth, all PlaSim simulations exhibit warmer conditions in the oceans between 30°S and 30°N latitude. This is particularly true for the PLASIM-ML simulation at T42 which, however, does not reproduce the same Arctic warming in 2005 relative to 1850 as the other PlaSim simulations and the EC-Earth simulation.

The dominant features emerging from the three maps of precipitation change obtained with PlaSim (Fig. 6) are the positive precipitation change in 2005 relative to 1850 over the equatorial Pacific, Atlantic, and Indian oceans, Oceania, and in the mid-latitudes of the northern hemisphere, around 60° latitude. The North Atlantic storm tracks are also clearly identifiable.

The PlaSim simulation at T42 shows a strong negative precipitation change along the south-eastern coast of the Asian continent, which is not found in the Plasim simulations at T21 but it is found, even if to a lesser extent, in the EC-Earth simulation. There are important differences between the EC-Earth spatial map of precipitation change and the three PlaSim maps; both positive and negative changes, moreover, are less pronounced in EC-Earth than in the three PlaSim simulations.

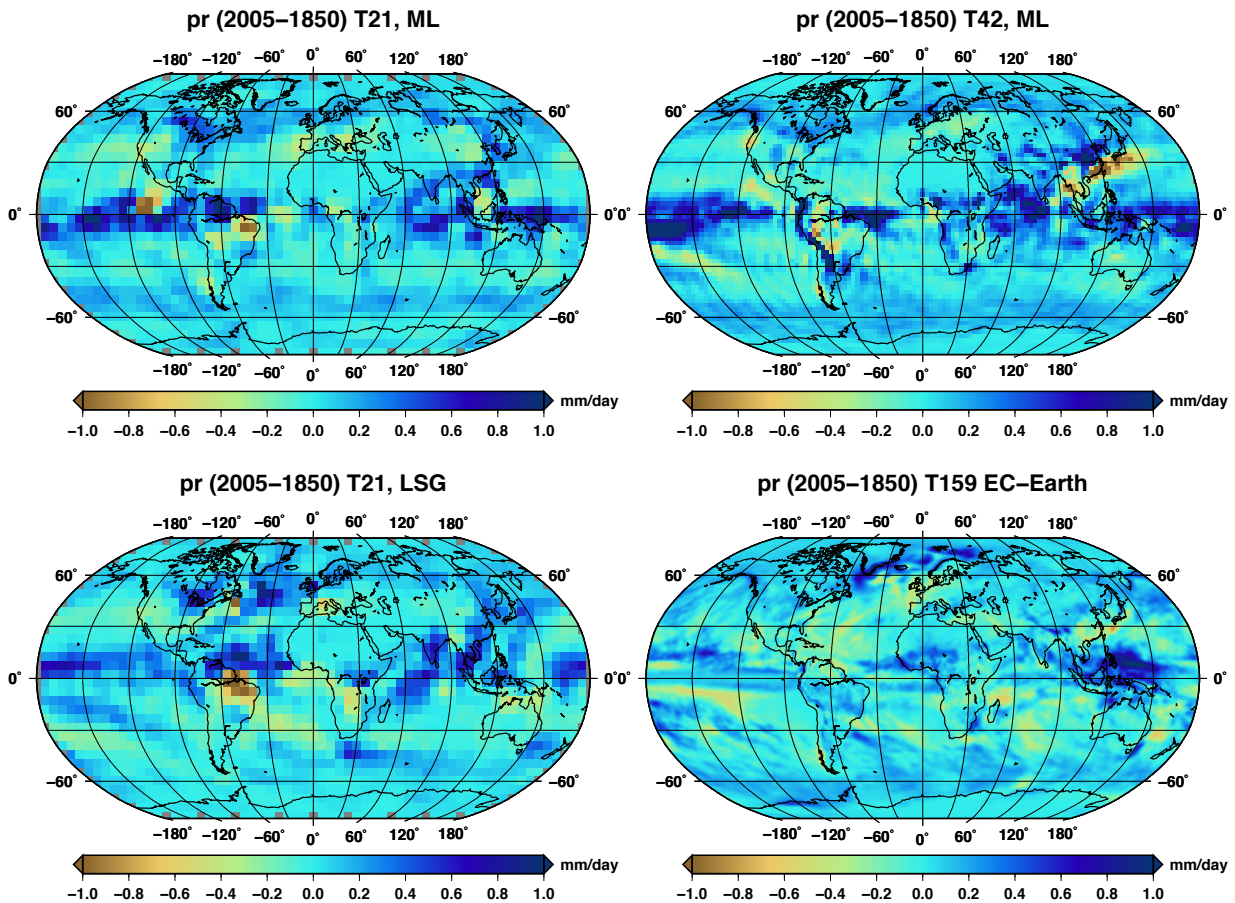


Fig. 6. The same as Figure 5, but for precipitation.

Zonal plots

The zonal mean plot of temperature and precipitation obtained from the perpetual PlaSim simulations and EC-Earth are shown in Fig. 7 and 8, respectively.

As for temperature, in the tropics, a better agreement is found between the EC-Earth and PlaSim/LSG outputs than between EC-Earth and PlaSim/ML, for both representative years. In the subtropics and higher latitudes, in general, all PlaSim simulations tend to underestimate precipitation with respect to EC-Earth.

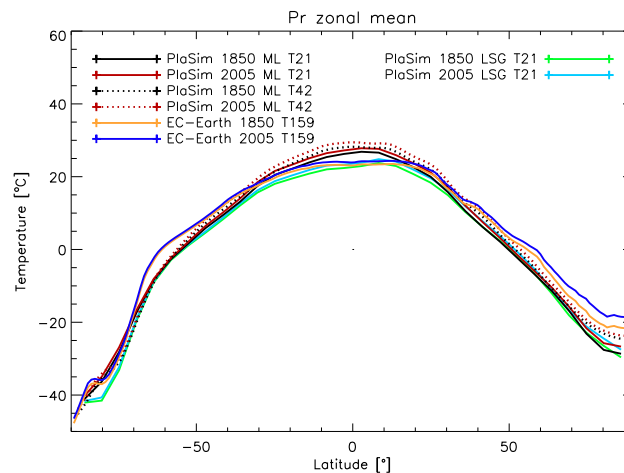


Fig. 7. Zonal mean plot of temperature from the perennial Plasim simulations at the different resolutions and ocean model configurations and from EC-Earth.

The various model simulations are less consistent with each other when the zonal mean precipitation, shown in Fig. 8, is considered. None of the PlaSim simulations displays the double peak structure in the tropics, associated with the ITCZ, which is instead represented in EC-Earth, consistently with the GPCP observations. The southern branch of the ITCZ is stronger in EC-Earth than in the observations. A very good agreement between EC-Earth and GPCP is found in the extra-tropics. In general, the PlaSim simulation outputs do not display the most remarkable features of the zonal mean precipitation found in the GPCP observations and in EC-Earth. Both simulations where PlaSim is coupled to the Mixed-Layer ocean tend to overestimate precipitation between 10°S and 10°N, while the PlaSim/LSG simulation gives precipitation amounts more similar to the observed ones and to the ones simulated by EC-Earth.

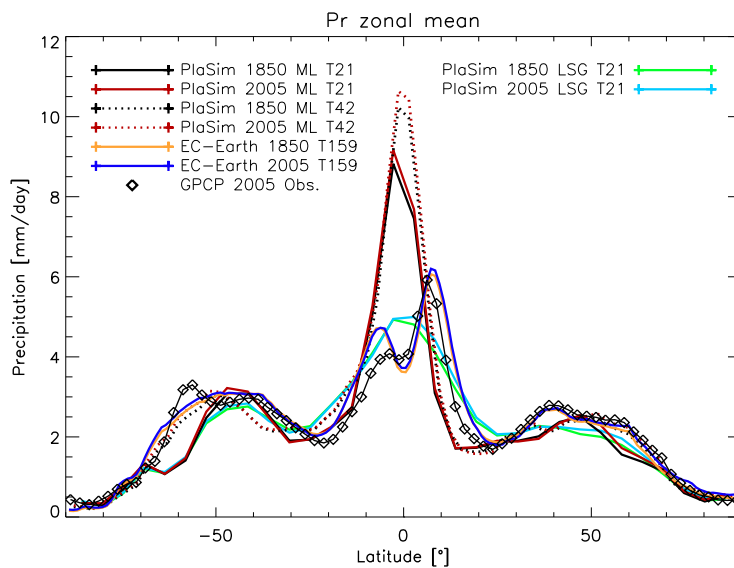


Fig. 8. The same as Figure 7, but for precipitation. GPCP 2005 data are also shown.

4. Analysis of transient runs: 150 years with historical CO2 forcing

Spatial maps

Figures 9 and 10 show the spatial distribution of the average temperature and precipitation change between the period (1986-2005) and the period (1850-1869) from the three PlaSim transient simulations (-ML at T21, -ML at T42 and -LSG at T21) and from EC-Earth.

As for the temperature (Fig. 9), a cooling pattern in the Southern Ocean is observed in the PlaSim-LSG simulation (bottom left panel) with respect to both T21 and T42 PlaSim-ML simulations and to EC-Earth. In general, PlaSim-LSG underestimates the warming pattern in the northern hemispheric land regions with respect to EC-Earth. The two PLASIM-ML simulations are more similar with each other over the oceans than over land areas.

In general, none of the PlaSim simulations compares very well with the picture provided by EC-Earth. The same consideration applies for the spatial pattern of the precipitation change, shown in Fig. 10. Even though some features of the precipitation change are roughly reproduced in the PlaSim simulation outputs compared to EC-Earth, it is difficult to clearly identify regions with similar patterns.

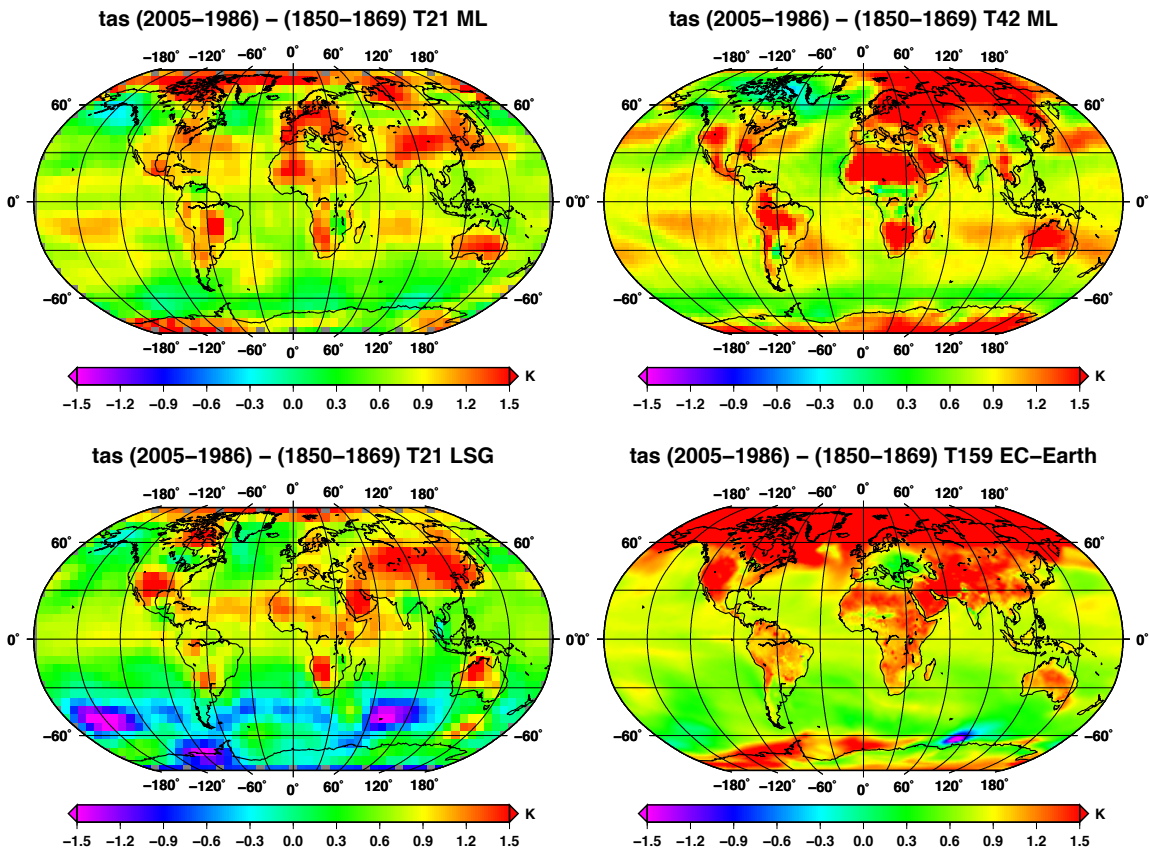


Fig. 9. Spatial maps of the surface temperature change obtained after subtracting the time-average over the period 1986-2005 from the time average over the period 1850-1869.

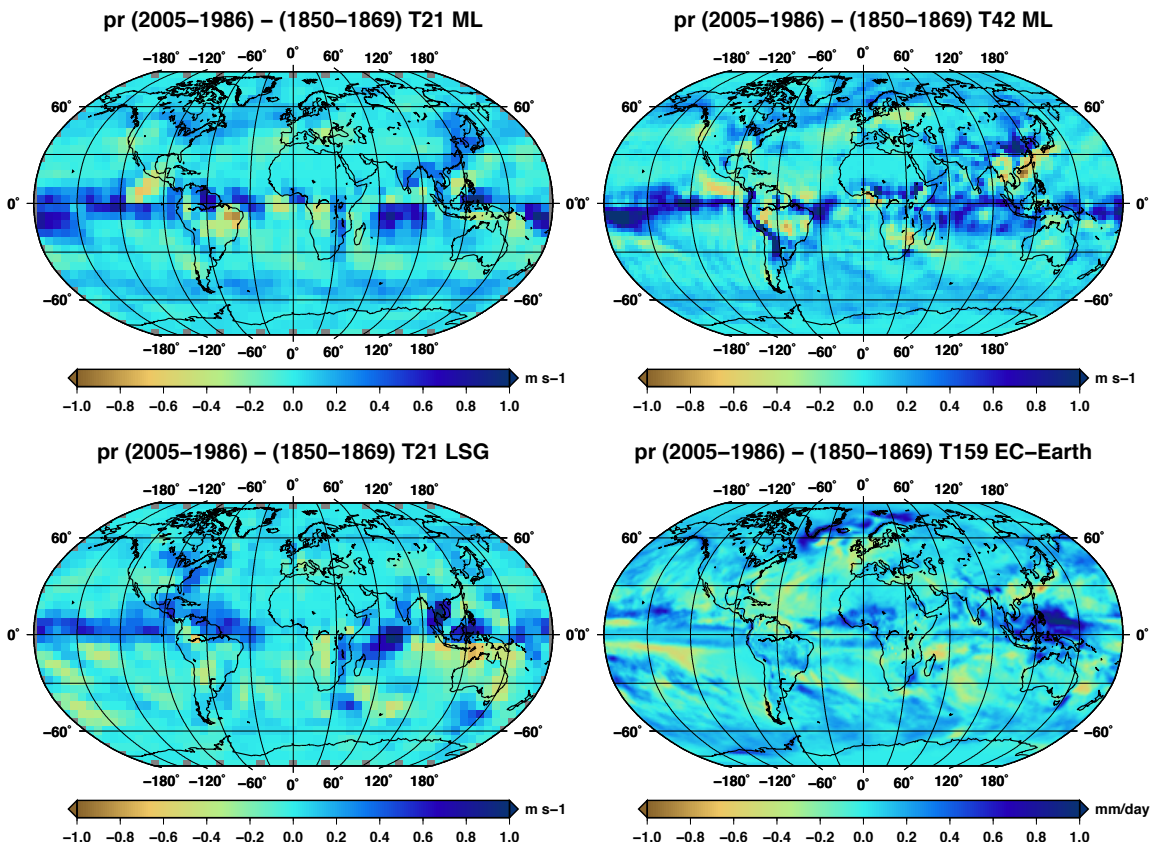


Fig. 10. The same as Fig. 9, but for precipitation.

Temperature time series

Figure 11 shows the globally-averaged temperature time series, from 1850 to 2005, obtained with the PlaSim-ML simulations at T21 (green line) and T42 (black line), PlaSim-LSG at T21 (red line), EC-Earth (blue line) and an ensemble of CMIP5 models (grey lines). As mentioned in the discussion of Fig. 9, Fig. 11 clearly shows the coldest temperatures simulated by PlaSim-LSG with respect to all other model simulation outputs shown in the figure. The PlaSim-ML simulation at T21 is also below the range simulated by the CMIP5 models (included the EC-Earth model) and lower than the PlaSim-ML simulation at T42. The latter is indeed well inside the CMIP5 model ensemble and produces, compared to EC-Earth (which is known to be affected, globally, by a cold bias; see Hazeleger et al., 2012), more realistic global mean surface temperatures.

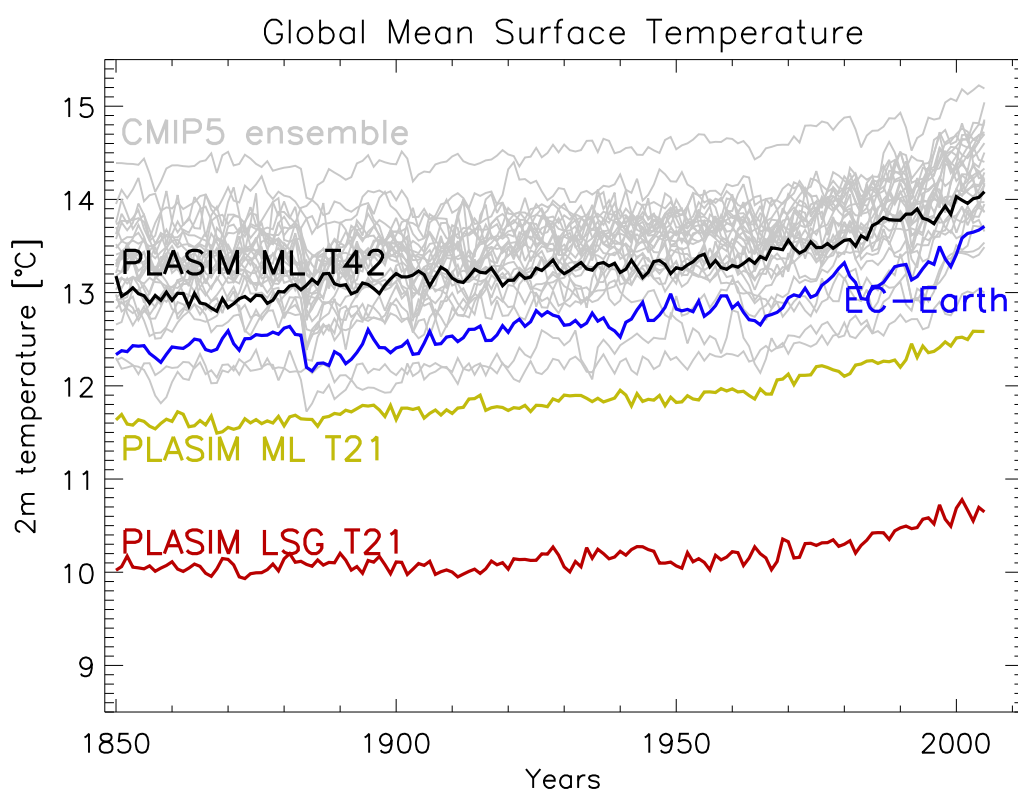


Fig. 11. Time series of global mean surface temperature from PlaSim (ML ocean), run at T21 (green) and T42 (black) resolutions, the EC-Earth model (blue) and the CMIP5 GCMs (light grey).

References

CLAUSSEN M., L. A. MYSAK, A. J. WEAVER, M. CRU- CIFIX, T. FICHEFET, M-F. LOUTRE, S. L. WEBER, J. ALCAMO, V. A. ALEXEEV, A. BERGER, R. CALOV, A. GANOPOLSKI, H. GOOSE, G. LOHMANN, F. LUNKEIT, I. I. MOKHOV, V. PETOUKHOV, P. STONE, Z. WANG, 2002: Earth system models of intermediate complexity: closing the gap in the spectrum of climate system models. – *Climate Dyn.* 18, 579–586.

MAIER-REIMER, E., MIKOLAJEWICZ, U., and HASSELMANN, K. 1993: Mean circulation of the Hamburg LSG OGCM and its sensitivity to the thermohaline surface forcing. *J. Phys. Oceanogr.*, 23, 731–757.

FRAEDRICH, K., E. KIRK, U. LUKSCH, and F. LUNKEIT, 2005: The Portable University Model of the Atmosphere (PUMA): Storm track dynamics and low frequency variability. *Meteorol. Zeitschrift*, 14:735-745.

HAZELEGER W, WANG X, SEVERIJNS C, STEFĂNESCU S, BINTANJA R, STERL A, WYSER K, SEMMLER T, YANG S, VAN DEN HURK B, VAN NOIJE T, VAN DER LINDEN E, VAN DER WIEL K, 2012: EC-Earth v2.2: description and validation of a new seamless earth system prediction model. *Clim Dyn* 39:2611-2629, DOI 10.1007/s00382-011-1228-5.

**D2.6.2f: "NEXTSNOW Special Project :
The snow cover detection algorithm 183-SCM", UR 1 -CNR-ISAC Bologna**

Prepared by: Sante Laviola
CNR-ISAC, Bologna

During the first year of the project the algorithm for snow cover detection called 183 Snow Cover Mask (183-SCM) has been applied over different geographical locations. The focus of this study was the evaluation of the algorithm performances and the quantification of weaknesses and strengths of the current computational scheme. To do that, a first validation over the Baltic Regions revealed the robustness of the method in the description of snow coverage over an almost flat terrain. Furthermore, the validation analysis shows that the 183-SCM performs much better when the snow mantle is thick while the retrieval over fresh snow is often misclassified. Future studies proposed in this project foresee the application of the methodology over the Alps where the complexity of terrain due to the orography and the presence of permanently frozen regions will be used to improve the current version of the algorithm.

1. A brief overview on satellite -derived snow cover

The retrieval of snow cover from remote sensing techniques in terms of frozen/no-frozen soil and of Snow Water Equivalent (SWE) is still a challenging problem. In general, the snow mantle can be identified from its conformity to the geographic features; in fact, it is quite easy to recognise the areas usually free of snow and those covered. Historically, the detection and mapping of snow coverage were realized by exploiting the high albedo of snow packs using visible and near-infrared sensors. Many techniques, based on a multispectral approach, have been developed to distinguish the contribution of snow mantle from other reflecting bodies such as low clouds (Kidder and Wu, 1984; 1987). Other methods based on the analysis of successive images to evaluate the cloud motion across the snowfield were associated to the multispectral analysis to better distinguish snow from low clouds. However, much of these techniques were limited only for daytime applications and in the presence of steady cloud coverage over the snow mantle the retrieval was not performed. The advent of satellite microwave radiometers open new opportunities for mapping snow covered terrain. The substantial transparency of clouds and the high penetration into the snow pack especially for lower window frequencies provide accurate information on the snow mantle both in terms of superficial features such as spatial distribution and of internal properties such as snow depth, grain size, and SWE (Chang et al., 1976, 1991; Hall et al., 1986; Foster et al., 1991, 1999). Thus, the high sensitivity of microwave to the metamorphosis of snow layers makes it possible the monitoring of the status of mantle emphasizing the presence of liquid water in the snowpack, which indicates the onset of melt (Kunzi et al, 1982).

Our approach is based on a combination of different microwave channels in the frequency range 89-190 GHz. Although, the penetrating capability into the snow mantle for these frequencies is lower than those around 10-40 GHz, we can exploit the high scattering signal by frozen particles and compacted snowflakes to retrieve the extension of snow coverage. Furthermore, the variation of surface emissivity due to the different water content of snow allows to classify the snow cover according to its wetness.

2. Datasets

Two different datasets have been used to describe the snow coverage over the Baltic Regions:

- The daily NESDIS-IMS used as ground “truth”.
 - The microwave data of the AMSU-B and MHS sensors on board to the NOAA satellites
- The study period was selected during the winter season 2009-2010 where snowfall storms started in the early October up to March with maximum coverage and thickness of the mantle in January-February. The daily NESDIS dataset has been obtained from the IMS archive in ASCII format with the spatial resolution of 4 km. The first step of processing analysis was the elaboration of data over the study areas and the remapping over a rectangular grid $0.15^\circ \times 0.15^\circ$ to be consistent with the nadir spatial resolution of the satellite data. The AMSU-B/MHS data used for the input to the 183-SCM were downloaded in level 11b from the NOAA-CLASS digital library and processed with the ATOVS and AVHRR Pre-processing Package (AAPP). Hence, in order to analyse *pixel-by-pixel* the two datasets the 183-SCM data were first remapped on the $0.15^\circ \times 0.15^\circ$ grid and in a second step all overpasses were combined to produce a 1-day snow cover mask.

3. Introduction to the method 183-SCM

The algorithm 183-SCM is a computational module for snow cover detection originally developed to remove the spurious signals from the rain rates retrieved with the 183-WSL method (Laviola and Levizzani, 2011; Laviola et al., 2013). Since the high similarity between the scattering signal by ice hydrometeors and that of frozen soils we developed a series of cascade tests to identify a snowy terrain and filter it out from the computation chain of rainfall. The 183-SCM, currently still in the testing stage, produces a snow cover mask per each satellite overpass, distinguishing between regions of wet and dry snow. The algorithm is physically based on the combination of two window frequencies at 89 GHz and 150 GHz with the quasi-opaque frequency at 190 GHz. The high sensitivity to the ice crystals on the surface of the window frequencies at 89 and 150 GHz combined with the scattered radiation at 190 GHz, which is typically observed over frozen soils, allows for an accurate identification of snow-covered terrain. In figure 1 a schematic representation of the 183-SCM algorithm is presented. As we can note, the snow cover detection algorithm exploits a cascade test based on three thresholds: $\Delta_{win} = (BT_{89} - BT_{150})$, $\Delta_{89} = (BT_{89} - BT_{190})$, and $\Delta_{150} = (BT_{150} - BT_{190})$. The first difference is particularly sensitive to the presence of rainy clouds so that it is used by the 183-WSL retrieval method to screen out all no-rainy pixels. Nevertheless, over snowy terrain it often occurs that scattering signal by the snowpack measured by Δ_{win} is quite similar to that by frozen hydrometeors and thus the algorithm produces a large number of false alarms due to the unrealistic selection of precipitating areas. For this reason, the microwave rainfall retrievals over frozen terrain are rather difficult or completely impossible. From the same figure 1, an example of incorrect classification of rain can be observed. During the snowstorm over Europe described in the figure the brightness temperatures at 89 and 150 GHz revealed a marked depression of signal corresponding to the snow mantle. Especially at 150 GHz, where the scattering of ice crystals is highly distinguishable, the snow particles deeply impact on the satellite signal with a detected value around 230 K. Therefore, as a consequence of that, the threshold Δ_{win} becomes greater than 3 K, which is the minimum value used in the 183-WSL retrieval procedure to classify a pixel over land as rainy. To mitigate the crude measurements of the Δ_{89} other thresholds are employed. Being the frequency at 190 GHz more sensitive to the absorption of water vapour in the first 2-3 km of atmosphere, the combination of this frequency with those at 89 and 150

GHz associated with the low temperature profiles characterizing the snowy conditions, senses the variation of the snow status in terms of hydration of the mantle. The Δ_{89} and Δ_{150} thresholds, being based on window frequencies accurately sense the surface emissivity variations and consequently support the detection of the soil features. In particular, it was found that the increasing of the water content in the snowpack tends to depress the threshold Δ_{89} more than the Δ_{150} while the latter threshold shows more attitudes to identify the dry snow areas. On these physical bases, the 183-SCM algorithm combining the three threshold contributions is capable to identify and characterize all pixels associated to snow cover for each satellite overpasses. This considerably improves the 183-WSL estimations of rainfall rates both reducing the number of misclassified rain areas and by better defining the domain of precipitating patterns (Laviola et al., 2013).

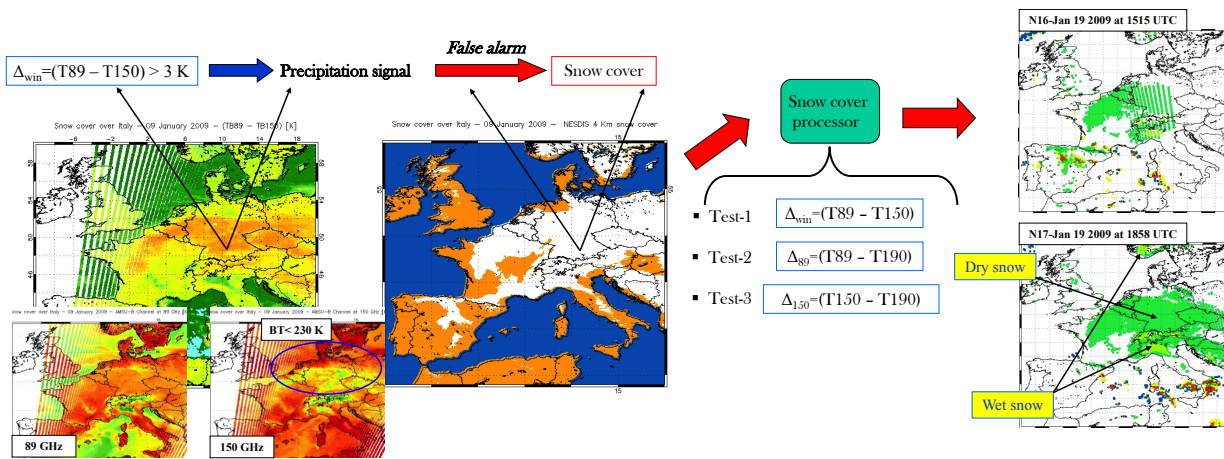


Fig. 1. Retrieval scheme of the 183-SCM algorithm. Two AMSU-B channels at 89 and 150 GHz are shown together with their combination (Δ_{win}), the NESDIS Interactive Multisensor Snow and Ice Mapping System (IMS) used as ground “truth”, the cascade tests of the 183-SCM and two snow cover maps for corresponding NOAA overpasses for 19 January 2009 at 1515 and 1858 UTC, respectively.

4. Validation analysis

The first validation analysis proposed here is based on the evaluation of discrepancies between the 183-SCM 1-day product and the corresponding NESDIS-IMS snow cover maps. Not yet specific statistics have been applied being this investigation a first step of a much more wide study. In figure 2 the results of the 183-SCM algorithm applied over the Scandinavian Peninsula during the winter season 2009-2010 are reported. The diagrams show the discrepancy analysis between the 1-day 183-SCM and the daily maps of NESDIS-IMS. In the first 2-months of the 2010 the discrepancy distribution trend tends to a general decrease while for the last 2-months of the year 2009 the tendency is inverted. This could be reasonably due to the presence of the previous snow mantle deposited during Oct-Dec, which makes the soil coverage more uniform. The scattering by frozen and thick old layers of snow deeply reduces radiation especially at 150 GHz with an enhancement of the algorithm performances. Green coloured figures correspond to the discrepancy best values indicated by the minimum in the diagrams. From these images it is rather clear that the majority of the detected snow is classified as fresh snow except in February when Scandinavia is covered by dry snow. Finally, the investigations revealed that large discrepancies affecting the snow retrievals are often associated with large amounts of cloud droplets and water vapour over the snowy terrains. Although scattering is generally stronger than absorption, in the 183-SCM frequencies the radiation absorbed

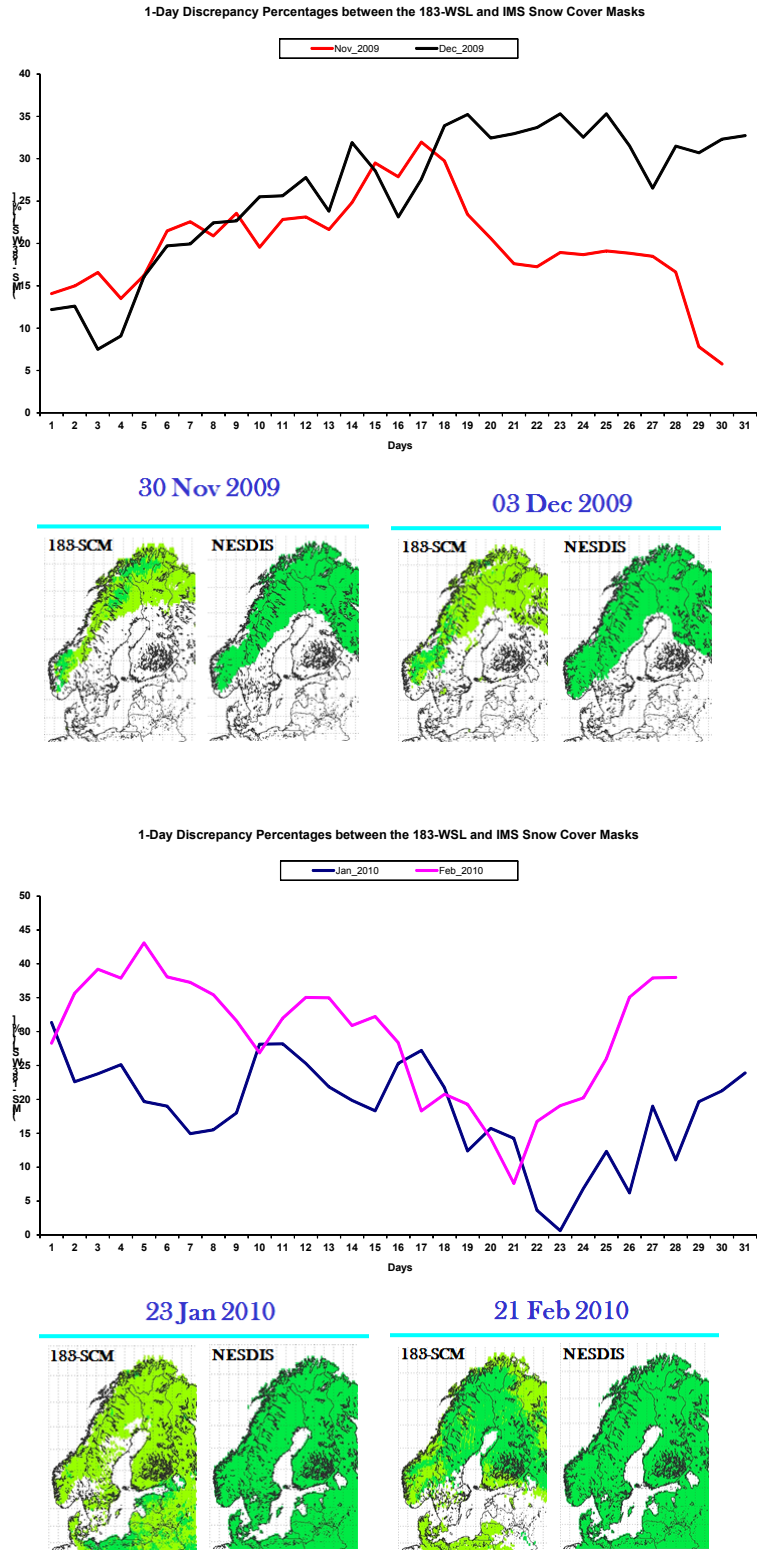


Fig. 2. Diagram of discrepancies between the 183-SCM and the NESDIS IMS used as “ground truth” for various winter months over the Scandinavian Peninsula. During November (red line) and December (black line) maximum discrepancies ranged in 5-33% and 12-35%, respectively whereas in January (blue line) and February (pink line) they were 0-30% and 7-45%. The best performances (minimum discrepancy) of the 183-SCM are also shown with dry (dark green) and wet (light green) snow.

by cloud aggregations could mask the light scattering from fresh snow cover thus forcing the misclassification of the retrieved pixels.

5. Limits and weaknesses of the current version of the algorithm

The current version of the 183-SCM algorithm is still in testing stage. Therefore, limits and weakness already known or find out during the validation process must be considered for future applications. The now existing critical points of the computational scheme can be summarized as follows:

- The 183-SCM algorithm can not be used for mountain with top higher than 2000 meters. In this domain, all pixels are systematically flagged as snow cover and then removed from the computational chain of rain rate. Thus, this missing information reflects the impossibility of the 183-WSL to retrieve orographic rainfall/snowfall for altitude greater than 2000 meters.

- In addition to the previous critical point, an improvement to the current version of the 183-SCM will be necessary based on the understanding of the impact of surface roughness on the signal from a snowy terrain. This is a crucial issue that could be mitigated by a combined analysis using a DEM and ground-based measurements.

- Low accuracy in the detection of fresh snow. The method has revealed low sensitivity to very thin snow mantle due to the low contrast between emission from unfrozen soil and light scattering by terrain with ice crystals deposited on top.

- The 183-SCM classifies the different contributions of the snowpack to the total radiation field as wet and dry snow on the basis of different surface emissivity. Although this discernment is, in general, quite difficult to realize because the scattering signal in the frequency range used in the algorithm is strictly linked to the variation of wetness. However, this classification ought to be validated with ground-based measurements.

- Low sensitivity to the changes of the snowpack physical state. Because of the intrinsic limits of the method (high frequencies are lesser penetrating into the mantle than those lower than 40 GHz) and the nowadays absence of calibration with in-site instruments, the 183-SCM method badly reproduces the real dynamics of the mantle metamorphosis. This is further reinforced by the low number of NOAA/MetOP-MHS overpasses, which is currently very limited.

6. Considerations and expected improvements from the project

In conclusion of this initial investigation of the 183-SCM performances, it must be said that the validation results reveal the robustness of the method to detect snow cover especially when the snowpack becomes more homogeneous and thick. This strength of the algorithm is strictly related to the physical mechanisms regulating the metamorphosis of snow mantle. The increasing of snow depth, which induces the compacting of mantle (high density) and the aggregation of crystals, widely increases the scattering of the upward radiation. Thus, the brightness temperature measured by satellite is drastically reduced and being this measure proportional to the thickness and density of snow mantle, the detection of coverage distribution is advantaged. Nevertheless, the first drawback of this approach is related to the choice of the frequencies. This means that, by using high frequencies to classify the snow cover the method suffers from a low

penetrating capability in the snowpack with respect to other approaches based on microwave frequencies lower than 40 GHz, which deeply penetrate the mantle. Therefore, the application of this approach to predict the snowmelt runoff needs to account for possible underestimations of the equivalent water content because this measure is substantially related to the top layers of the sheet. Furthermore, the limits and weaknesses reported in section 5 could be reduced or at least mitigated with a new calibration of the thresholds on the basis of ground-based measurements. Thus, the upward scattered radiation by snowpack measured by satellite could be linked to in-site measurements of the snow superficial and inner properties such as depth and water content, density and grain size, stratification of volume snow-land both in terms of snow state and of physical conditions of first layers of land (wet or frozen). For these reasons, the contest of the Strategic Project NextSnow offers a good occasion to improve the method extending its detection skills in other domains. In fact, the application of the 183-SCM over the Alps where the tops of mountains are often over 2000 meters and dense snow gauge measurements are presently available, could be exploited to retune the sensitivity thresholds of the 183-SCM. As a consequence of that, the support of a new frequency into the original scheme of the algorithm can be considered. The AMSU-B/MHS opaque channel 4 at frequency 186 GHz changes its weighting function from the nominal value of about 6 km toward the lower atmospheric layers proportionally to the vertical amount of water vapour. Thus, the implementation of this frequency could introduce a new radiometric information which can reduce the current dependency of the method to the knowledge of topography provided by a DEM.

References

- CHANG A.T.C., P. GLOERSEN, T. SCHMUGGE, T.T. WILHEIT, H.J. ZWALLY, 1976: Microwave emission from snow and glacier ice. *Journal of Glaciology*, 16, 74, 2311-2319.
- CHANG A.T.C., J.L. FOSTER, A. RANGO, 1991: Utilization of surface cover composition to improve the microwave determination of snow water equivalent in a mountain basin. *International Journal of Remote Sensing*, 12, 2311-2319.
- FOSTER J.L., D.K. HALL, A.T.C. CHANG, A. RANGO, 1991: Derivation of snow water equivalent in boreal forests using microwave radiometry. *Arctic*, 44, 174-152.
- FOSTER J.L., A. CHANG, D.K. HALL, A. RANGO, W. WERGIN, E. ERBE, 1999: Effects of snow crystal shape on the scattering of passive microwave radiation. *IEEE Trans. Geosci. Remote Sensing*, 37, 2, 1165-1168.
- HALL D.K., A.T.C. CHANG, J.L. FOSTER, 1986: Detection of the depth-hoar layer in the snowpack of the Arctic Coastal Plain of Alaska. *Journal of Glaciology*, 32, 110, 87-94.
- KIDDER, S. T., and H. T. WU, 1984: Dramatic contrast between low clouds and snow cover in daytime 3,7 μm imagery. *Mon. Wea. Rev.*, 112, 2345-2346.
- KIDDER, S. T., and H. T. WU, 1987: A multi-spectral study of the St. Louis area under snow-covered conditions using NOAA-7 AVHRR data. *Remote Sens. Environ.*, 22, 158-172.
- KUNZI K. F., PATIL S. and ROTT H., 1982: Snow-covered parameters retrieved from NIMBUS-7 SMMR data. *IEEE Trans. Geosci. Remote Sensing* GE-20, 452-67.
- LAVIOLA S., and V. LEVIZZANI, 2011: The 183-WSL fast rain rate retrieval algorithm. Part I: Retrieval design. *Atmos. Res.*, 99, 443-461.

LAVIOLA, S., V. LEVIZZANI, E. CATTANI, and C. Kidd, 2013: The 183-WSL fast rainrate retrieval algorithm. Part II: Validation using ground radar measurements. *Atmos. Res.*, 134, 77-86.

Glossary

AAPP	ATOVS and AVHRR Pre-processing Package
AMSU	Advanced Microwave Sounding Unit
ASCII	American Standard Code for Information Interchange
BT	Brightness Temperature
CLASS	Comprehensive Large Array-data Stewardship System (NOAA)
CNR	National Research Council of Italy
DEM	Digital Elevation Model
ISAC	Institute of Atmospheric Sciences and Climate (CNR)
IMS	Interactive Multisensor Snow and Ice Mapping System
MetOP programme	Meteorological Operational of the EUMETSAT Polar System
NESDIS	National Environmental Satellite, Data and Information Service (NOAA)
NOAA	National Oceanic and Atmospheric Administration
SWE	Snow Water Equivalent
183-SCM	183-Snow Cover Mask (module of the 183-WSL method)
183-WSL	Water vapor Strong Lines at 183 GHz method